

Full length article

Characteristic deformation microstructure evolution and deformation mechanisms in face-centered cubic high/medium entropy alloys

Shuhei Yoshida^{a,b,*}, Rui Fu^c, Wu Gong^d, Takuto Ikeuchi^a, Yu Bai^{b,e}, Zongqiang Feng^c, Guilin Wu^c, Akinobu Shibata^{b,f}, Niels Hansen^{g,1}, Xiaoxu Huang^c, Nobuhiro Tsuji^{a,b}

^a Department of Materials Science and Engineering, Kyoto University, Yoshida-honmachi, Sakyo-ku, Kyoto 606-8501, Japan

^b Elements Strategy Initiative for Structural Materials (ESISM), Kyoto University, Yoshida-honmachi, Sakyo-ku, Kyoto 606-8501, Japan

^c International Joint Laboratory for Light Alloys (MOE), College of Materials Science and Engineering, Chongqing University, Chongqing 400044, China

^d J-PARC Center, Japan Atomic Energy Agency, 2-4, Shirane Shirakata, Tokai, Ibaraki 319-1195, Japan

^e School of Materials Science and Engineering, Dalian University of Technology, 2 Linggong Rd., Ganjingzi District, 116024 Dalian, China

^f Research Center for Structural Materials, National Institute for Materials Science, 1-2-1 Sengen, Tsukuba, Ibaraki 305-0047, Japan

^g Technical University of Denmark, Risø campus, DK-4000 Roskilde, Denmark

ARTICLE INFO

Keywords:

High/medium entropy alloys
Dislocation structure
Deformation twinning
Strain hardening
3D characterization

ABSTRACT

Face-centered cubic (FCC) high/medium entropy alloys (HEAs/MEAs), novel multi-principal element alloys, are known to exhibit exceptional mechanical properties at room temperature; however, the origin is still elusive. Here, we report the deformation microstructure evolutions in a tensile-deformed $\text{Co}_{20}\text{Cr}_{40}\text{Ni}_{40}$ representative MEA and $\text{Co}_{60}\text{Ni}_{40}$ alloy, a conventional binary alloy for comparison. These FCC alloys have high/low friction stresses, fundamental resistance to dislocation glide in solid solutions, respectively, and share similar other material properties, including stacking fault energy. The $\text{Co}_{20}\text{Cr}_{40}\text{Ni}_{40}$ MEA exhibited higher yield strength and work-hardening ability than in the $\text{Co}_{60}\text{Ni}_{40}$ alloy. Deformation microstructures in the $\text{Co}_{60}\text{Ni}_{40}$ alloy were marked by the presence of coarse dislocation cells (DCs) regardless of grain orientation and a few deformation twins (DTs) in grains with the tensile axis (TA) near $\langle 1\ 1\ 1 \rangle$. In contrast, the MEA developed three distinct deformation microstructures depending on grain orientations: fine DCs in grains with the TA near $\langle 1\ 0\ 0 \rangle$, planar dislocation structure (PDS) in grains with other orientations, and a high density of DTs along with PDS in grains oriented $\langle 1\ 1\ 1 \rangle$. Three-dimensional electron tomography revealed that PDS in the MEA confined dislocations within specific $\{1\ 1\ 1\}$ planes, indicating suppression of cross-slip of screw dislocations and dynamic recovery. In-situ X-ray diffraction during tensile deformation showed a higher dislocation density in the MEA than in the $\text{Co}_{60}\text{Ni}_{40}$ alloy. These findings demonstrate that FCC HEAs/MEAs with high friction stresses naturally develop unique deformation microstructures which is beneficial for realizing superior mechanical properties compared to conventional materials.

1. Introduction

Dislocations play an essential role in plastic deformation of metallic materials. If an applied shear stress is higher than the critical resolved shear stress (CRSS) of materials, dislocations start moving, resulting in macroscopic yielding. Furthermore, as deformation proceeds, dislocations and other crystal defects such as stacking faults and deformation twins (DTs) spontaneously form characteristic morphologies, so-called dislocation microstructures or deformation microstructures. Previous studies have shown that, with increasing strain, dislocation

microstructures evolve into some distinct patterns depending on various factors such as crystal structure, activated slip/twinning systems, crystallographic orientation, stacking fault energy (SFE), and grain size. For example, Huang *et al.* have found that dislocation microstructures formed in individual grains of tensile-deformed pure Al [1] and Cu [2] (with face-centered cubic (FCC) structure) having coarse grain sizes could be classified into three types depending on the tensile axis (TA) orientation of the grains: (Type I) extended and straight dislocation boundaries along $\{1\ 1\ 1\}$ planes; (Type II) randomly oriented dislocation cell boundaries defining a three-dimensional cell structure; (Type III) a

* Corresponding author.

E-mail address: yoshida.shuhei.5s@kyoto-u.ac.jp (S. Yoshida).

¹ Dr. Niels Hansen of Technical University of Denmark passed away on 19 Augst 2021.

structure similar to Type I but having extended boundaries deviating from $\{1\ 1\ 1\}$ planes. This classification was found to be consistent with deformation microstructures observed in single-crystals having similar orientations. It was also found that Type II structure could be more elongated and aligned along TA with decreasing SFE [3]. The differences in these three kinds of deformation microstructures have been attributed to differences in activated slip systems in each grain, leading to different dislocation reactions [4–6]. Le *et al.* [7] reported deformation microstructures of tensile-deformed Al with various mean grain sizes. They found that, with decreasing the grain size, Type I and III structures were gradually mixed, and the materials having a mean grain size smaller than several micrometers only showed dislocation cells (DCs) and tangled dislocation structures. This suggests that grain boundaries also affect the formation of deformation microstructures in fine-grained materials. Most importantly, these deformation microstructures are responsible for work-hardening of metals. Hughes and Hansen [8] showed that flow stress of metals could be explained by theoretical formulas, in which inputs were structural parameters extracted from actual deformation microstructures such as sizes of DCs and their boundary misorientations. Therefore, careful characterization of deformation microstructure is essential to understand the underlying physics of plastic deformation in metals.

Compared with pure FCC metals, superior mechanical properties (high strength and large ductility) and different deformation microstructures have been reported for high-alloy systems, such as high-Mn steels [9,10], Hadfield steels [11–14], and high-nitrogen steels [15–18]. Gutierrez-Urrutia *et al.* [9,10] investigated the deformation microstructures in a tensile-deformed Fe-Mn-Al-C twinning-induced plasticity (TWIP) steel (SFE: $\gamma = 63\text{ mJm}^{-2}$). They reported planar slip of dislocations along specific $\{1\ 1\ 1\}$ planes and subsequent formation of planar dislocation structure (PDS) with the Taylor lattice. With increasing strain, development of DCs in TA $\sim//$ $\langle 1\ 0\ 0 \rangle$ oriented grains, and fine cell blocks (CBs), in which PDS was subdivided by incidental dislocation boundaries (IDBs), were observed in other grains. In addition, DTs were observed in TA $\sim//$ $\langle 1\ 1\ 1 \rangle$ oriented grains. Work-hardening behavior of the TWIP steel was found to be directly linked to the deformation microstructure development. Similar results were reported by Ueji *et al.* for an Fe-Mn-Al-Si TWIP steel ($\gamma < 40\text{ mJm}^{-2}$) [19]. Deformation microstructure development in high/medium entropy alloys (HEAs/MEAs), which are new classes of high-alloy systems composed of five or more / four or fewer alloying elements with near-equimolar composition [20–25], has been studied by several groups recently. Laplanche *et al.* investigated deformation microstructures of polycrystalline CoCrFeMnNi HEA [26] and CoCrNi MEA [27], and subsequently many groups also reported the deformation microstructure evolution in various CoCrNi-based HEAs/MEAs, as reviewed by Lu *et al.* [28], for instance. Their deformation microstructures were found to be very similar to that seen in the TWIP steels (i.e., the formation of PDS, fine CBs, DCs, and DTs). Similar results have also been reported for single-crystalline FCC HEAs with similar crystal orientations [29–37]. It is generally believed that the formation of PDS and fine CBs is attributed to the low SFE [38] or short-range ordering (SRO) [39], which makes it difficult for dissociated screw dislocations lying on $\{1\ 1\ 1\}$ planes to cross-slip. However, some TWIP steels exhibiting PDS do not show any evidence of SRO and have SFEs close to that of pure Cu [10] that generally shows non-planar dislocation microstructures [2]. This implies that there must be additional factors contributing to the deformation microstructure development that leads to the superior strength-ductility balance in FCC high-alloy systems, other than the SFE. Despite the great efforts described above, quantitative understanding of the effect of alloying on deformation microstructure development and its relation to mechanical properties has not been attained owing to the lack of systematic studies. Elucidating such additional factors can be of great importance for a broader understanding of deformation mechanisms in various FCC metals and alloys.

One important difference between high-alloy systems and dilute

systems (including pure metals) can be a magnitude of the yield strength. High-alloy systems are essentially heterogeneous at an atomic scale because different alloying elements occupy different lattice sites, and the crystal lattice can be severely distorted owing to the differences in atomic sizes. Our previous studies [40–42] have revealed that the high yield strength of high-alloy systems like HEAs and MEAs is attributed to the high friction stresses (fundamental resistance to dislocation motion in solid solutions), measured as the intercept values of the Hall-Petch relationships [41–48]. This is because of the interaction between elastic field of dislocations and the severe lattice distortion (large atomic size misfits of alloying elements). Thus, the high friction stress (high yield strength) can be characterized as an essential characteristic of high-alloy systems. On the other hand, an increase in yield strength and flow stress generally results in a decrease in tensile ductility of materials due to the plastic instability effect [49]. This contrasts with the fact that FCC high-alloy systems normally exhibit superior strength-ductility balance compared to conventional materials. Thus, in high-alloy systems with high friction stresses like HEAs and MEAs, there must be a special mechanism that leads to superior mechanical properties, which might also be related to the deformation microstructure evolution.

Based on this idea, we hypothesized that high friction stress might be a key to clarify the additional factors affecting deformation microstructure evolution and resultant mechanical properties in FCC high-alloy systems. For FCC HEAs and MEAs having high friction stress such as CoCrFeMnNi HEA [50] and CoCrNi MEA [40], Co-Ni binary system is a very suitable benchmark for comparison because it has low friction stresses close to that of pure Ni [40] and very similar other material properties (e.g., elastic constants, lattice constant, and melting temperature) [51,52]. Also, their SFEs can be easily tailored over a wide range by changing the atomic fractions of Co and Ni [53]. Thus, in the present study, we quantitatively compared deformation behavior and deformation microstructure evolution in a Co₆₀Ni₄₀ (at.%) alloy and a Co₂₀Cr₄₀Ni₄₀ (at.%) MEA, which have the lowest and highest friction stresses, respectively, among subsystems of the CoCrFeMnNi HEA [41, 52–56] and have other comparable material properties including SFE, by using state-of-the-art two-/three-dimensional microstructure analysis in transmission electron microscopy (TEM) and in-situ synchrotron X-ray diffraction (XRD) during tensile deformation. The ultimate goal of this study is to elucidate the essential characteristics of deformation microstructure evolution in FCC high-alloy systems and their relation to superior mechanical properties achieving both high strength and large ductility.

2. Experimental procedures

2.1. Materials processing

Ingots of Co₆₀Ni₄₀ alloy and Co₂₀Cr₄₀Ni₄₀ MEA were fabricated by vacuum arc-melting of pure metals (purity > 99.9 wt.%) under an inert gas (high-purity argon) atmosphere. After melting, they were cooled in a water-cooled copper mold and flipped and re-melted five times to improve compositional homogeneity. Subsequently, the ingots were cold-rolled to a 30% reduction in thickness and homogenized at 1100 °C for 24 h. Then, the homogenized plate of the Co₆₀Ni₄₀ alloy and the Co₂₀Cr₄₀Ni₄₀ MEA were further cold-rolled to a 92% reduction in thickness and annealed at 750 °C for 120 s and 850 °C for 3.6 ks, respectively. These processes yielded fully-recrystallized microstructures of FCC single phase having similar mean grain sizes of about 3 μm (including annealing twins) in the two alloys.

2.2. Microstructure observation of undeformed materials

Microstructure observation of the undeformed materials was performed by using a scanning electron microscope (SEM) (JSM-7800F, JEOL Ltd.) equipped with a back-scattering electron detector (BSE)

operated at an acceleration voltage of 25 kV and a probe current of 1.0 nA. The specimens for observation were mechanically polished with SiC sandpapers having grit sizes between #1000 and #4000. Subsequently, they were electrically polished in a solution of 10 vol.% HClO₄ and 90 vol.% C₂H₅OH at 30 V for 15 s at room temperature.

2.3. Characterization of mechanical properties

Tensile tests were conducted at room temperature to evaluate the mechanical properties. Small-scaled dog-bone specimens with a gauge length of 2 mm and a gauge cross-section of 1 mm × 0.5 mm were cut from the recrystallized materials. Tensile deformation was applied with an initial strain rate of $8.3 \times 10^{-4} \text{ s}^{-1}$ until fracture. In-situ strain measurements during tensile deformation were performed by using the digital image correlation (DIC) method [57]. It has already been verified in our previous studies [40,41] that tensile tests with such small-scaled specimens and DIC methods yield highly reliable stress-strain curves, comparable to those measured using standard-size specimens with an extensometer. To investigate the deformation microstructure evolution, tensile deformation was interrupted at engineering strains of 2, 10, 30, and 50%.

2.4. Microstructure observation of deformed materials

Deformation microstructure observations were conducted by using TEM (JEM-2100 / 2100F, JEOL Ltd.) equipped with a bright field (BF) detector and an annular dark field (ADF) detector for scanning TEM (STEM), operated at 200 kV. The TEM observation plane was parallel to the sheet surface plane of the tensile specimens. Foil specimens for TEM observations were mechanically polished until the thickness reached 50 μm by using SiC sandpapers with #1000 – #4000 grit sizes. Subsequently, they were electrically polished in a solution of 10 vol.% HClO₄, 20 vol.% glycerin, and 70 vol.% CH₃OH at 15 V and 243 K by using a twin-jet electropolishing machine (Tenupol-5, Struers Ltd.). Diffraction contrast of lattice defects was observed under the two-beam conditions in both TEM and STEM [58–60]. The camera length of STEM detectors and spot size of the electron beam were set to 40 cm and 1 nm, respectively, which were the optimal conditions for the deformation microstructure observations of the materials in the microscopes. Crystallographic orientation of each observed grain was determined based on the Kikuchi patterns formed by convergent electron beam diffraction and analyzed by a semi-automatic procedure [61,62]. For each deformation condition, about 20–30 grains from the two foil specimens were examined to obtain statistically reliable results.

2.5. Three-dimensional characterization of deformation microstructure

TEM-based electron tomography (ET) [63] was performed to reveal three-dimensional morphology of dislocation structures in the tensile-deformed MEA specimens. In this technique, diffraction contrast images of dislocations are acquired with a wide range of tilt angles. Then, the three-dimensional structure of dislocations is reconstructed by mathematical algorithms. As the diffraction contrast of dislocations is strictly dependent on the diffraction condition (*g*-vector), all images need to be taken with the same *g*-vector where targeted dislocations are visible (Readers can also refer Refs. [64–66] for more details on the technique).

ET of 5% tensile-deformed Co₂₀Cr₄₀Ni₄₀ MEA was conducted in a TEM (TECNAI G20, FEI) operated at 200 kV. The thin foils for ET were fabricated under the same conditions as those described in Section 2.4. The specimen was attached to a high-angle triple-axis TEM holder (HATA-holder) (Mel-Build) with maximum tilt angles of ± 80° and ± 7.5° in the X- and Y-axes, respectively. We kept a stable two-beam diffraction condition with a *g*-vector of *g* = ⟨3 1 1⟩ during tilting. A series of weak-beam dark-field (WBDF) TEM images was acquired in a tilt-angle range of ± 50° along the X-axis with an interval of 1.0°. The

acquired images were aligned by Inspect3D (Thermo Fischer Scientific), and the dislocation structures were then reconstructed by the weighted back-projection algorithm [67] with Avizo (Thermo Fischer Scientific).

2.6. In-situ synchrotron X-ray diffraction measurement during tensile deformation

To quantify deformation behavior of the materials, we also conducted in-situ high-energy XRD measurements during tensile deformation at the beamline 46XU of a synchrotron radiation facility, Super Photon ring – 8 GeV (SPring-8) in Hyogo, Japan. Plate-type dog-bone specimens having a gauge length of 10 mm and a gauge cross-section of 3 mm × 0.5 mm were cut from the same recrystallized materials as described in Section 2.1. Tensile deformation was applied in a load frame attached to a goniometer at room temperature with an initial strain rate of $8.3 \times 10^{-4} \text{ s}^{-1}$ until fracture. Incident X-ray beam with an energy of 30 keV (wavelength of 0.0413 nm) and a spot size of 0.5 mm (length) × 0.5 mm (width) was irradiated on the center of the gauge part of the tensile specimens. Transmission-diffracted X-ray beams were detected by a one-dimensional semiconductor detector (MYTHEM, Dectris) covering a 2θ range of 5° - 35°. The exposure time (data acquisition time) for each profile was set to 1.0 s to achieve a better signal-noise ratio, and diffraction profiles were collected continuously during the tensile testing. The incident X-ray beam was precisely monochromated by a double mirror silicon monochromator. A camera length between the specimens and the detector was adjusted by a computer-controlled four-axis goniometer. Also, the direction of the incident beam was adjusted to be perpendicular to the tensile specimen surface. The system was calibrated by using a well-annealed standard CeO₂ sample before the measurements.

The peaks were fitted by the pseudo-Voigt function to obtain the peak position and integral intensity. Dislocation density and planar fault probability of the materials were estimated by the convolutional multiple whole profile fitting (CMWP) method [68]. For the analysis, {*h k l*} (*h k l* = 1 1 1, 2 0 0, 3 1 1, 2 2 2, and 3 3 1) peaks of FCC structure were used. It should be noted that grains where diffraction occurred are oriented close to TA ~// ⟨*h k l*⟩ owing to the small 2θ values. One must be aware that XRD line profiles of the undeformed specimens can be broadened owing to the intrinsic severe lattice distortion of high-alloy systems, distorting the crystal lattice. This can result in overestimation of the dislocation density. Thus, the XRD profiles of the deformed specimens were deconvoluted in the CMWP program based on the XRD profiles of the undeformed specimens to remove such an effect of severe lattice distortion, as proposed by Heczal et al. [69].

3. Results

3.1. Material properties and microstructure of undeformed materials

The material properties of the Co₆₀Ni₄₀ alloy and Co₂₀Cr₄₀Ni₄₀ MEA are listed in Table 1. The lattice constants of FCC structure were determined to be 0.3535 nm and 0.3559 nm for the Co₆₀Ni₄₀ alloy and

Table 1

Material properties of the Co₆₀Ni₄₀ alloy and Co₂₀Cr₄₀Ni₄₀ MEA measured experimentally and extracted from literature [41,51,53,54].

Material properties	Co ₆₀ Ni ₄₀ alloy	Co ₂₀ Cr ₄₀ Ni ₄₀ MEA
Crystal structure	FCC single phase	
Lattice constant, <i>a</i> / nm	0.3535	0.3559
Stacking fault energy, <i>γ</i> / mJm ⁻²	30 ± 5	
Homologous temperature at room temperature, <i>T</i> / <i>T</i> _m	0.170	0.173
Shear modulus, <i>G</i> / GPa	86	87
Mean grain size, <i>d</i> / μm	3.10	2.79
Hall-Petch slope, <i>k</i> / MPa m ^{1/2}	181	168
Friction stress, <i>σ</i> ₀ / MPa	52	280

$\text{Co}_{20}\text{Cr}_{40}\text{Ni}_{40}$ MEA, respectively, based on the synchrotron XRD measurements before deformation. The friction stresses of the $\text{Co}_{60}\text{Ni}_{40}$ alloy and $\text{Co}_{20}\text{Cr}_{40}\text{Ni}_{40}$ MEA were determined to be 52 MPa and 280 MPa, respectively, at room temperature based on our previous studies [40,41,55]. Figs. 1(a) and (b) show SEM-BSE micrographs of initial microstructures of the $\text{Co}_{60}\text{Ni}_{40}$ and $\text{Co}_{20}\text{Cr}_{40}\text{Ni}_{40}$, respectively. Equiaxed grains with profuse annealing twin boundaries were seen in both alloys. Textures of these materials were close to random, given the characteristics of recrystallization texture in FCC metals [70]. Mean grain sizes of the $\text{Co}_{60}\text{Ni}_{40}$ alloy and $\text{Co}_{20}\text{Cr}_{40}\text{Ni}_{40}$ MEA were found to be 3.10 μm and 2.79 μm by the intercept method. Other material properties (SFE, homologous temperature at room temperature, shear modulus, and the Hall-Petch slope) were extracted from the literature [41,42,51,71]. It should be noted that the accuracy of the SFE values reported in the literature [53,54] was verified again based on separation distance of dissociated dislocations measured by our own WBDF-TEM observations [72], and possible artifacts due to the high friction stress of the MEA, pointed out by some recent studies [73–75], were technically avoided by observing multiple grains with different orientations (see supplementary materials for the details). It is also noteworthy that the elastic anisotropies of the two alloys, which are related to atomic bonding state in crystals, were experimentally estimated to be comparable, as described later in Section 3.5. Therefore, average energy landscape of generalized SFE and resultant twinability [76] of the materials are expected to be comparable, according to the literature [77–80]. The data above clearly indicate that the material properties of the $\text{Co}_{60}\text{Ni}_{40}$ alloy and $\text{Co}_{20}\text{Cr}_{40}\text{Ni}_{40}$ MEA were very close, except for the friction stresses.

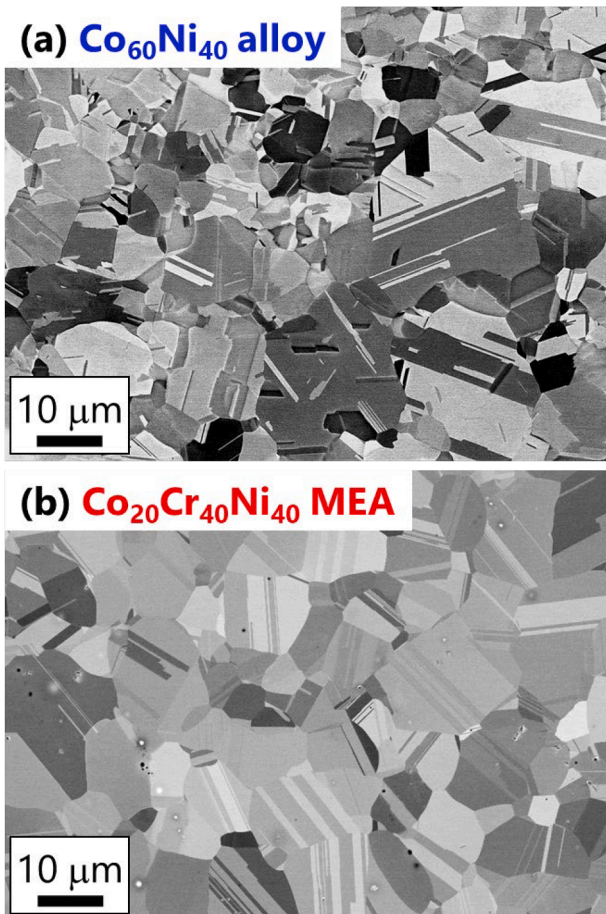


Fig. 1. SEM-BSE micrographs of (a) the $\text{Co}_{60}\text{Ni}_{40}$ alloy and (b) $\text{Co}_{20}\text{Cr}_{40}\text{Ni}_{40}$ MEA processed by cold-rolling and subsequent annealing at 750 °C for 120 s and 850 °C for 3.6 ks, respectively.

3.2. Macroscopic tensile deformation behavior

Fig. 2(a) plots the engineering stress – engineering strain curves of the $\text{Co}_{60}\text{Ni}_{40}$ alloy and $\text{Co}_{20}\text{Cr}_{40}\text{Ni}_{40}$ MEA. The yield strength (0.2% proof stress) of the $\text{Co}_{60}\text{Ni}_{40}$ alloy and $\text{Co}_{20}\text{Cr}_{40}\text{Ni}_{40}$ MEA were 140 MPa and 375 MPa, respectively. The contribution of grain size to the yield strength (the Hall-Petch effect), $kd^{-1/2}$, can be calculated as 103 MPa and 101 MPa for the $\text{Co}_{60}\text{Ni}_{40}$ alloy and $\text{Co}_{20}\text{Cr}_{40}\text{Ni}_{40}$ MEA, respectively, based on their nearly identical Hall-Petch slopes, as shown in Table 1. Therefore, the difference in the yield strength (235 MPa) corresponds well with the difference in the friction stress (= 228 MPa) in the materials. The ultimate tensile strengths of the $\text{Co}_{60}\text{Ni}_{40}$ alloy and $\text{Co}_{20}\text{Cr}_{40}\text{Ni}_{40}$ MEA were 419 MPa and 685 MPa, respectively. Generally, there is a trade-off relationship between strength and ductility of materials. Thus, materials having higher strength tend to exhibit lower ductility. However, despite the difference in the flow stress, interestingly, the two alloys showed almost the same ductility (fractured at $e \sim$

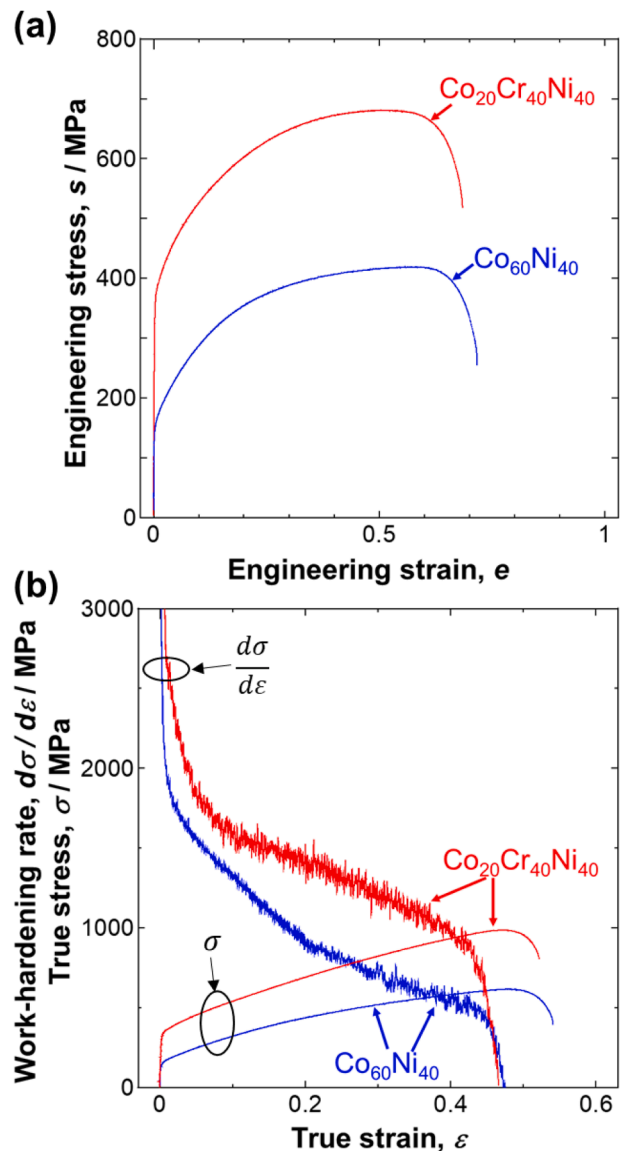


Fig. 2. (a) Engineering stress-engineering strain curves of the $\text{Co}_{60}\text{Ni}_{40}$ alloy (blue) and $\text{Co}_{20}\text{Cr}_{40}\text{Ni}_{40}$ MEA (red). (b) Work-hardening rate-true strain curves of the $\text{Co}_{60}\text{Ni}_{40}$ alloy (blue) and $\text{Co}_{20}\text{Cr}_{40}\text{Ni}_{40}$ MEA (red) plotted together with their true stress-true strain curves. (For interpretation of the references to colour in this figure legend, the reader is referred to the web version of this article.)

0.72). Fig. 2(b) shows work-hardening rate - true strain curves of the $\text{Co}_{60}\text{Ni}_{40}$ alloy and $\text{Co}_{20}\text{Cr}_{40}\text{Ni}_{40}$ MEA plotted together with the true stress - true strain curves. It was found that the work-hardening rate of the $\text{Co}_{20}\text{Cr}_{40}\text{Ni}_{40}$ MEA was higher than that of the $\text{Co}_{60}\text{Ni}_{40}$ alloy. The crossing points between the work-hardening rate curves and the true stress - true strain curves are where necking occurs, satisfying the plastic instability condition [49], expressed as

$$\frac{d\sigma}{d\varepsilon} \leq \sigma, \quad (1)$$

where σ and ε are true stress and true strain, respectively. Eq. (1) suggests that necking was retarded in the $\text{Co}_{20}\text{Cr}_{40}\text{Ni}_{40}$ MEA owing to the higher work-hardening ability, resulting in a similar uniform and fracture elongations as in the $\text{Co}_{60}\text{Ni}_{40}$ alloy.

3.3. Orientation dependence of deformation microstructure evolution

To explain the difference in the work-hardening ability between the two alloys, we investigated their deformation microstructure evolution. Typical TEM observations are shown in Fig. 3 and Fig. 4 for the $\text{Co}_{60}\text{Ni}_{40}$ alloy and $\text{Co}_{20}\text{Cr}_{40}\text{Ni}_{40}$ MEA, respectively, which are described in the following.

3.3.1. $\text{Co}_{60}\text{Ni}_{40}$ alloy

Fig. 3 shows deformation microstructure evolution in the tensile-deformed $\text{Co}_{60}\text{Ni}_{40}$ alloy with different applied strains. The microstructures could be classified into two types, Type A and Type A-T, as shown in Fig. 5(a). Type A structure is characterized by DCs that developed from loose cells or tangled dislocations in the early stage of deformation ($e \sim 5\%$) into well-defined cells with increasing strain. The cell size of Type A grains is ~ 500 nm at a strain of 10%, decreasing to ~ 300 nm at $e = 50\%$. Type A-T structure is characterized by a mixture of DCs and nanoscale DTs (the lower-right image in Fig. 3) that develops only at $e \sim 50\%$. It is also noted that the sizes of the DCs in the Type A-T grains were smaller (e.g., ~ 200 nm at a strain of 30%) than those in Type A. As shown in Fig. 5(a), it is seen that Type A structure develops

regardless of the grain orientation, while Type A-T structure forms only in the grains oriented close to TA $\sim // \langle 111 \rangle$. This indicates that the formation of DTs has a strong grain orientation dependence and occurs only in grains with higher dislocation density (smaller cell size) where more frequent dislocation reactions for the nucleation of DTs are expected, as discussed later in Section 4.1.2. The appearance of DCs was similar to the Type II grains in tensile-deformed pure Cu, but the microstructures of Types I and III were not observed. This might be due to the effect of the small grain size, i.e., constraint effect by grain boundaries, resulting in activation of various slip systems and formation of DCs, as reported for pure Al [7]. Further study is necessary to clarify the grain size dependence of deformation microstructure in low SFE materials, which is beyond the scope of this paper and is our on-going work.

3.3.2. $\text{Co}_{20}\text{Cr}_{40}\text{Ni}_{40}$ MEA

Fig. 4 presents the deformation microstructure evolution in the tensile-deformed $\text{Co}_{20}\text{Cr}_{40}\text{Ni}_{40}$ MEA with different strains. It was found that the microstructure could be classified into three types depending on the grain orientation, as shown in Fig. 5(b): (Type A) Randomly-tangled dislocations were seen at the early stage of deformation, and DCs with a size of several tens of nanometers developed with increasing strain in TA $\sim // \langle 100 \rangle$ oriented grains; (Type B) Planar slip of dislocations was seen at the early stage, and PDS subsequently formed along one of $\{111\}$ planes in most grains except for those oriented such that TA $\sim // \langle 100 \rangle$; (Type B-T) PDS developed in more than two $\{111\}$ planes, and DTs with a thickness of several nanometers started nucleating after an applied strain of $e \sim 10\%$ in TA $\sim // \langle 111 \rangle$ oriented grains. It seemed that the number fraction of DTs increased with increasing applied strain, while the thickness did not change significantly. It should be noted that the PDS and DTs observed in Type B and B-T grains were mainly lying on a $\{111\}$ plane belonging to the $\langle 110 \rangle \{111\}$ slip system having the highest Schmid factor (the primary slip system). The deformation microstructures and their orientation dependence in this alloy closely resembled those reported in both single-crystals and poly-crystals of other FCC high-alloy systems, as described in Section 1. Additionally, we note that, in our preliminary work on the same MEA tensile-deformed at

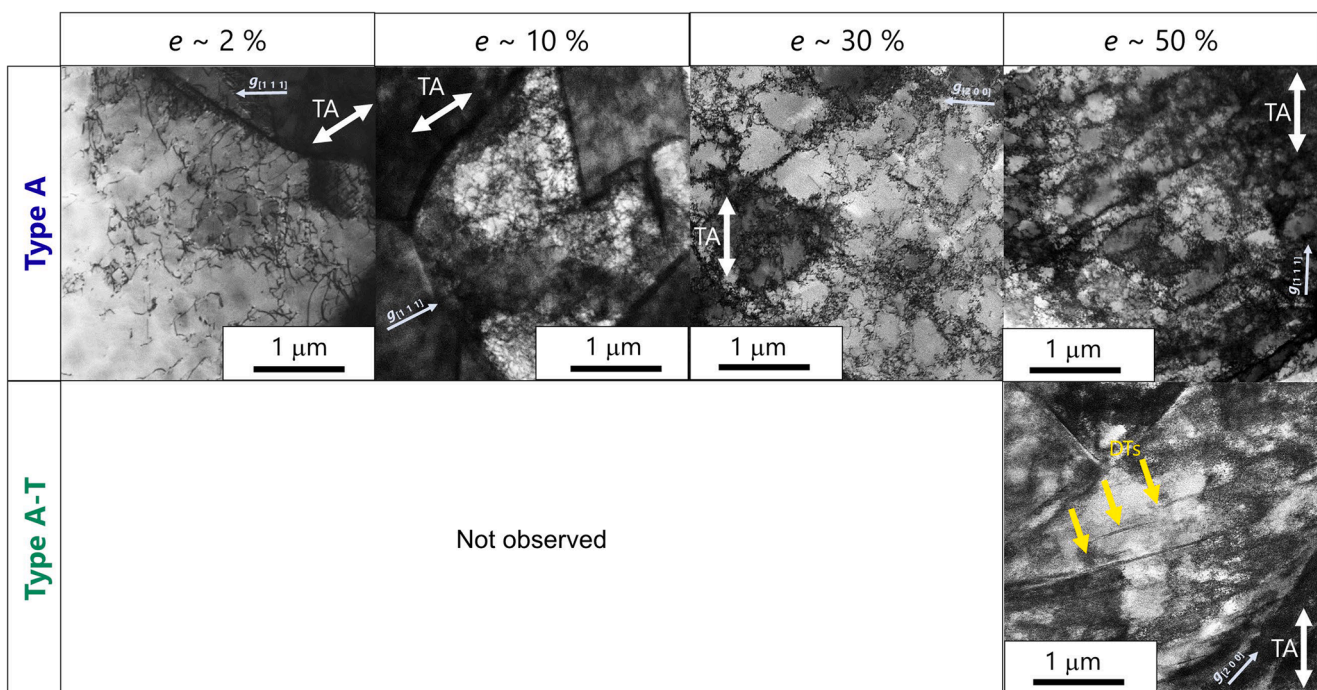


Fig. 3. STEM micrographs of the two types of deformation microstructure (Types A and A-T) of the $\text{Co}_{60}\text{Ni}_{40}$ alloy at different applied strains (e) of up to $\sim 50\%$. TA and g-vector ($g_{[h k l]}$) are indicated in each image. Type A-T microstructure was observed only at $e \sim 50\%$. The plate-shaped defects indicated by yellow arrows in Type A-T are DTs.

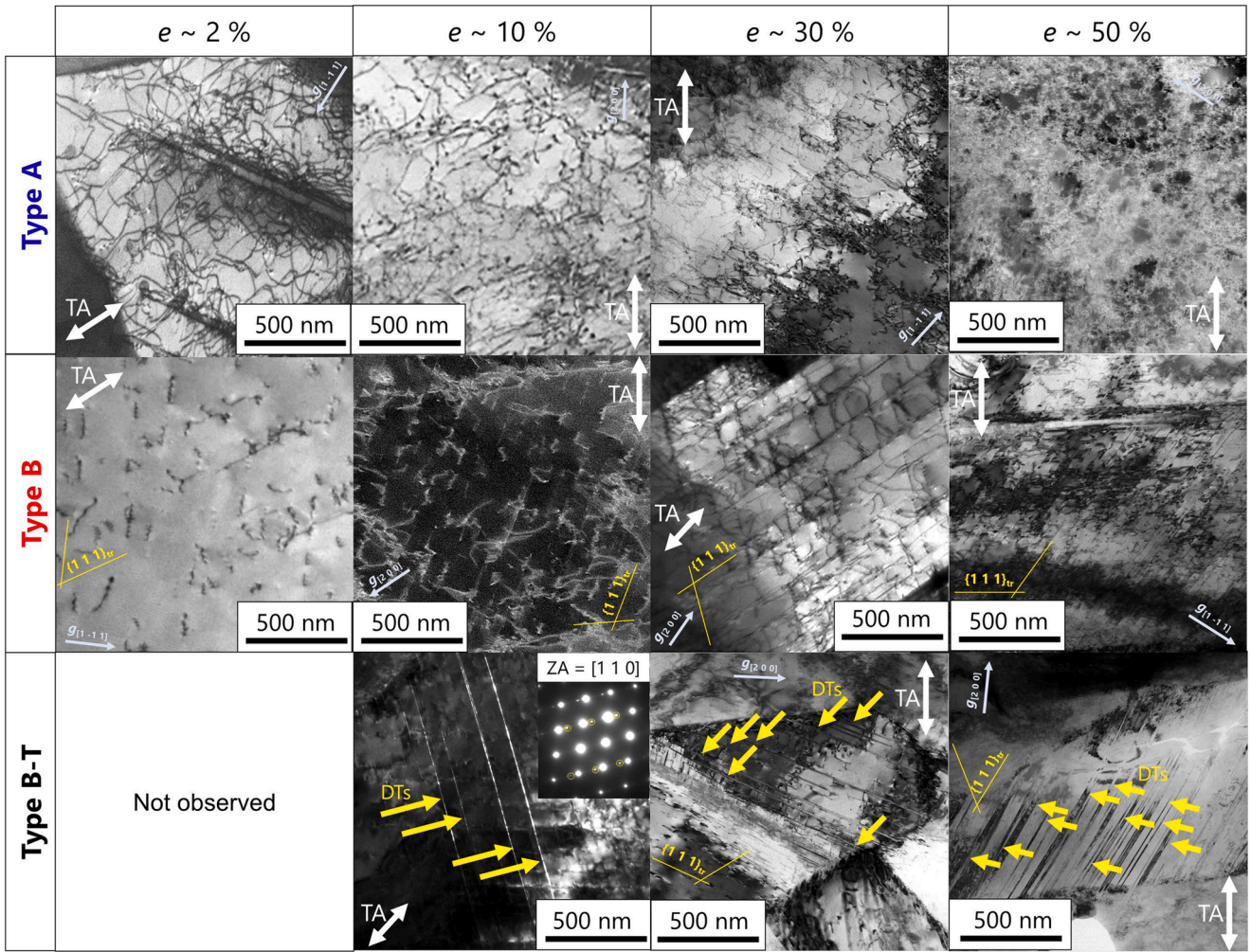


Fig. 4. TEM/STEM micrographs of the three types of deformation microstructure (Types A, B, and B-T) observed in the $\text{Co}_{20}\text{Cr}_{40}\text{Ni}_{40}$ MEA at different applied strains e of up to $\sim 50\%$. TA and g -vector ($g_{[h k l]}$) are indicated in each image. The plate-shaped defects indicated by yellow arrows in the $e \sim 10\text{--}50\%$ images for Type B-T are DTs. The inset in the dark-field TEM image of Type-B-T at $e \sim 10\%$ is an SAD pattern showing the presence of twins ($2n 0 0$ reflections (n : integer) of twins), as indicated by yellow circles. (For interpretation of the references to colour in this figure legend, the reader is referred to the web version of this article.)

room temperature [56], we observed a very small fraction of deformation-induced martensite with a hexagonal close-packed structure after necking. However, since the phase fraction is very small ($\sim 0.4\%$ volume fraction after fracture), the martensitic transformation can have negligible impacts on the evolution of deformation microstructures and the macroscopic mechanical properties of the alloy, and the effect is therefore omitted in this study.

3.4. Three-dimensional structure of PDS in the $\text{Co}_{20}\text{Cr}_{40}\text{Ni}_{40}$ MEA

Three-dimensional structure of the PDS in Type B grains of the $\text{Co}_{20}\text{Cr}_{40}\text{Ni}_{40}$ MEA was revealed by ET. Reconstructed dislocation structure of a Type B grain in the 5% deformed $\text{Co}_{20}\text{Cr}_{40}\text{Ni}_{40}$ MEA can be seen in **supplementary videos 1** (aligned image series) and **2** (reconstructed structure by the weighted back-projection algorithm). Figs. 6 (a-i) show WBDF-TEM images of the dislocation structure taken at different tilt-angles. Based on the images taken with different g -vectors, we determined the Burgers vectors of the dislocations according to the $g\cdot b$ criteria [81]. It should be noted that dislocations in the material dissociated into two Shockley partials and an intrinsic stacking fault (ISF), owing to its low SFE. For example, in Fig. 6(a), the slip systems of some of the dislocations were identified to be the following:

$$\text{Slip system 1 (red)} : \frac{a}{2} [1 0 \bar{1}] (1 1 1) \rightarrow \frac{a}{6} [2 \bar{1} \bar{1}] (1 1 1) + \text{ISF} \\ + \frac{a}{6} [1 1 \bar{2}] (1 1 1)$$

$$\text{Slip system 2 (blue)} : \frac{a}{2} [\bar{1} 1 0] (1 1 \bar{1}) \rightarrow \frac{a}{6} [\bar{1} 2 1] (1 1 \bar{1}) + \text{ISF} \\ + \frac{a}{6} [\bar{2} 1 \bar{1}] (1 1 \bar{1})$$

These dislocations are colored red and blue in Fig. 6(a'), while the rest undetermined dislocations are colored white. We found that dislocations belonging to these slip systems were confined in their slip planes, forming PDS, suggesting difficulty in cross-slip of screw dislocations and dynamic recovery. Edge-on views of the dislocations of the slip systems 1 and 2 aligned along the slip planes could be found in Figs. 6(f) and (c), respectively. Owing to the planar structure of the dislocations, these dislocations lying on the two different $\{1 1 1\}$ planes intersected each other, resulting in a formation of stair-rod immobile dislocations [82]. For instance, one Lomer-Cottrell dislocation with the Burgers vector of $\langle 1 1 0 \rangle$ was found, as indicated by the orange line in Fig. 6(a'), possibly due to dislocation reaction of

$$\frac{a}{6} [2 \bar{1} \bar{1}] (1 1 1) + \frac{a}{6} [\bar{1} 2 1] (1 1 \bar{1}) \rightarrow \frac{a}{6} [1 1 0] (0 0 1).$$

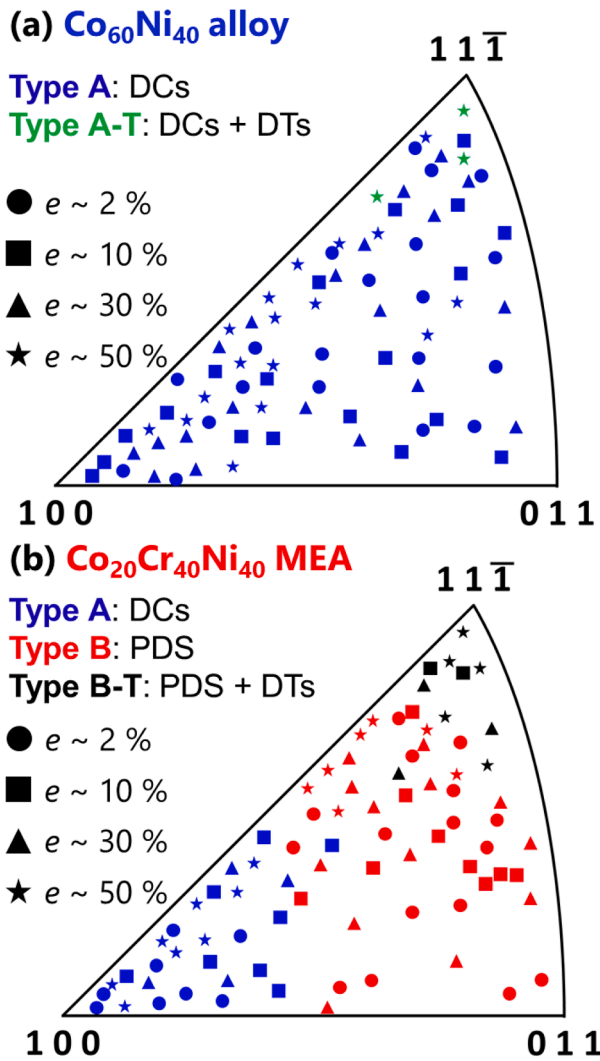


Fig. 5. Types of deformation microstructures in (a) the Co₆₀Ni₄₀ alloy and (b) Co₂₀Cr₄₀Ni₄₀ MEA classified according to the grain orientation against TA and applied strain. The blue and green data points represent grains having DCs and DCs + DTs, respectively. The red and black data points indicate grains having PDS and PDS + DTs, respectively. (For interpretation of the references to colour in this figure legend, the reader is referred to the web version of this article.)

Generally, inhibited dynamic recovery and the formation of such immobile dislocations during deformation contribute to a rapid increase in dislocation density and nucleation of DTs, which leads to a higher work-hardening ability [82,83], as discussed in Section 4 later.

3.5. Internal stress, texture, and defect density evolution during deformation

Since the structural information obtained by TEM was very local and qualitative, we investigated the deformation behavior through in-situ high-energy XRD measurements during tensile deformation. With increasing applied strain, all peaks shifted and broadened. In addition, intensity of each peak changed (see supplementary information). Based on shift in each peak, elastic deformation in grains having similar orientations can be determined [83]. Elastic strain (ϵ_{hkl}) in grains oriented to TA $\sim // \langle h k l \rangle$ is calculated as

$$\epsilon_{hkl} = \frac{d_{hkl} - d_{hkl}^0}{d_{hkl}^0}, \quad (2)$$

where d_{hkl} and d_{hkl}^0 are lattice spacing of $\{h k l\}$ planes during deformation and before deformation, respectively. By multiplying a diffraction elastic modulus (E_{hkl}), internal stress (σ_{hkl}) in grains oriented to TA $\sim // \langle h k l \rangle$ is calculated by

$$\sigma_{hkl} = E_{hkl} \epsilon_{hkl}. \quad (3)$$

It should be noted that the E_{hkl} can be determined by assuming that $\sigma_{hkl} = \sigma$ (applied stress) during elastic deformation [84]. We estimated the E_{hkl} of the Co₆₀Ni₄₀ alloy and Co₂₀Cr₄₀Ni₄₀ MEA as presented in Table 2. As the E_{hkl} values of these alloys are comparable, their elastic constants and anisotropies are expected to be also similar [85]. These E_{hkl} values are also close to those of other FCC high-alloy systems with low SFE reported previously (e.g., HEAs/MEAs and austenitic steels [84–87]). In Fig. 7(a), we show the internal stress in grains of the Co₆₀Ni₄₀ alloy and Co₂₀Cr₄₀Ni₄₀ MEA oriented to TA $\sim // \langle 1 1 1 \rangle$, $\langle 2 0 0 \rangle$, and $\langle 3 1 1 \rangle$ as a function of applied true strain, calculated based on stroke of the tensile test machine. It was found that the internal stress development in the Co₆₀Ni₄₀ alloy was almost independent of $\langle h k l \rangle$, while, in the Co₂₀Cr₄₀Ni₄₀ MEA, the internal stress varied depending on the orientation. This suggests that the deformation microstructures evolution in the Co₆₀Ni₄₀ alloy is relatively homogeneous, while those in the Co₂₀Cr₄₀Ni₄₀ MEA is heterogeneous (i.e., orientation-dependent). This was well consistent with the results of the deformation microstructure observations (Section 3.3). Fig. 7(b) shows a ratio of integral intensity of $\{1 1 1\}$ and $\{2 0 0\}$ peaks (I_{111}/I_{200}) of the Co₆₀Ni₄₀ alloy and Co₂₀Cr₄₀Ni₄₀ MEA as a function of applied true strain. It can be seen that the I_{111}/I_{200} of the Co₆₀Ni₄₀ alloy increased monotonically with increasing applied strain, while that of the Co₂₀Cr₄₀Ni₄₀ MEA saturated and slightly decreased above a strain of $\sim 20\%$. This behavior suggests that the fraction of DTs in the Co₂₀Cr₄₀Ni₄₀ MEA is larger than that in the Co₆₀Ni₄₀ alloy, leading to the different texture development in these two alloys [85]. This was also consistent with the results of the deformation microstructure observations. Fig. 7(c) plots planar fault probability (P_{pf}), an indicator calculated by the CMWP showing the abundance of ISFs on $\{1 1 1\}$ planes in FCC crystals, as a function of the applied strain. P_{pf} increased monotonically with increasing applied strain in both alloys, though the increase was more rapid in the Co₂₀Cr₄₀Ni₄₀ MEA. Just before necking ($e \sim 0.5$), the P_{pf} of the Co₂₀Cr₄₀Ni₄₀ MEA ($P_{pf} = 0.0330$) was about five times larger than that of the Co₆₀Ni₄₀ alloy ($P_{pf} = 0.0065$). This suggests that stacking faults in the Co₂₀Cr₄₀Ni₄₀ MEA are more abundant than those in the Co₆₀Ni₄₀ alloy. Fig. 7(d) shows dislocation densities in the Co₆₀Ni₄₀ alloy and Co₂₀Cr₄₀Ni₄₀ MEA calculated by the CMWP as a function of applied strain. It is seen that, with increasing applied strain, the dislocation density in the Co₂₀Cr₄₀Ni₄₀ MEA increased more rapidly than in the Co₆₀Ni₄₀, leading to a value roughly three times higher in the Co₂₀Cr₄₀Ni₄₀ MEA ($8.5 \times 10^{14} \text{ m}^{-2}$) than in the Co₆₀Ni₄₀ alloy ($3.1 \times 10^{14} \text{ m}^{-2}$). This was attributed to the inhibited dynamic recovery in the Co₂₀Cr₄₀Ni₄₀ MEA, as described in Section 3.4.

4. Discussion

4.1. Microstructure evolution in Co₆₀Ni₄₀ alloy and Co₂₀Cr₄₀Ni₄₀ MEA

Even though the Co₆₀Ni₄₀ alloy and Co₂₀Cr₄₀Ni₄₀ MEA have similar material properties, except for their friction stresses, they exhibited different behavior in terms of deformation microstructure evolution. In particular, the formation of the planar structure of dislocations (Types B and B-T) suggests that cross-slip of screw dislocations is more suppressed in the Co₂₀Cr₄₀Ni₄₀ MEA than in the Co₆₀Ni₄₀ alloy. Such differences in the deformation microstructure evolution have typically been attributed to differences in SFE or SRO. However, that cannot be the case in the present study since the material properties, including SFE, were unified in these two alloys, and no evidence of SRO was found in the Co₂₀Cr₄₀Ni₄₀ MEA. Thus, hereafter, we shall discuss possible reasons for

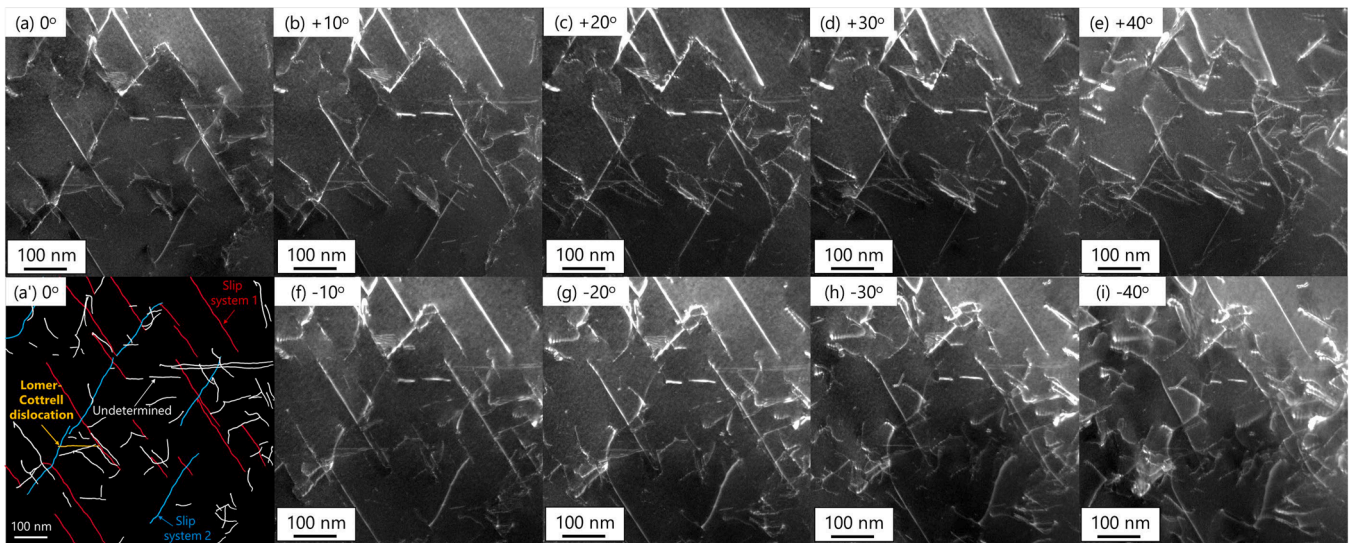


Fig. 6. (a – i) WBDF images of the Type B microstructure in the $\text{Co}_{20}\text{Cr}_{40}\text{Ni}_{40}$ MEA with $e \sim 5\%$, taken under different tilt angles of the X-axis ($\pm 40^\circ$). (a') Types of dislocations shown in (a) determined by the TEM analysis. The red and blue lines are dislocations lying on two different slip planes. The orange line is the Lomer-Cottrell dislocation. The white lines are dislocations belonging to undetermined slip systems. (For interpretation of the references to colour in this figure legend, the reader is referred to the web version of this article.)

Table 2

Diffraction elastic moduli (E_{hkl}) of the $\text{Co}_{60}\text{Ni}_{40}$ alloy and $\text{Co}_{20}\text{Cr}_{40}\text{Ni}_{40}$ MEA determined by in-situ XRD during tensile deformation.

Materials	E_{111}	E_{200}	E_{311}
$\text{Co}_{60}\text{Ni}_{40}$ alloy	245 GPa	131 GPa	200 GPa
$\text{Co}_{20}\text{Cr}_{40}\text{Ni}_{40}$ MEA	254 GPa	139 GPa	191 GPa

the difference in the deformation microstructure evolution in the two materials based on the difference in the friction stresses, which we thought might be a key to understand the difference in the deformation behaviors.

4.1.1. Dislocation microstructure evolution

4.1.1.1. Stress-induced variation of stacking fault width. In FCC crystals with low SFEs, perfect dislocations dissociate into two Shockley partial dislocations. Since these two partial dislocations have different Burgers vectors, the Schmid factors and resolved shear stress acting on the leading and trailing dislocations are not always identical. Figs. 8(a) and (b) show TA orientation dependence of the Schmid factor of leading ($a/6 [2 \ -1 \ -1] (1 \ 1 \ 1)$) and trailing partial dislocations ($a/6 [1 \ 1 \ -2] (1 \ 1 \ 1)$), respectively, dissociated from perfect dislocations belonging to the primary slip system ($a/2 [1 \ 0 \ -1] (1 \ 1 \ 1)$), where perfect dislocations have the highest Schmid factor). If the Schmid factor of the leading partial (m_{LP}) is larger than that of the trailing partial (m_{TP}) (the positive part in Fig. 8(c)), the width of stacking faults increases upon tensile loading due to the difference in the resolved shear stress acting on the partials. In other words, SFE in the crystal apparently decreases mechanically, and cross-slip of screw dislocations (dynamic recovery) becomes difficult. On the other hand, if m_{LP} is smaller than m_{TP} (the negative part in Fig. 8(c)), the width of stacking faults decreases, and SFE increases apparently upon tensile loading. Thus, cross-slip of screw dislocations (dynamic recovery) becomes easy. This is presumably why, in the $\text{Co}_{60}\text{Ni}_{40}$ alloy, the size of the DCs in Type A-T grains (TA $\sim // \langle 1 \ 1 \ 1 \rangle$) was smaller (i.e., dislocation density was higher because of the lower effective SFE (apparent SFE)) than that of Type A grains. According to Copley and Kear [88] and Kestenbach [89], an effective SFE (γ_{Eff}) under a tensile stress of σ is calculated by

$$\gamma_{\text{Eff}} = \gamma_0 - \frac{m_{LP} - m_{TP}}{2} \sigma b_p, \quad (4)$$

where γ_0 and b_p are respectively a SFE without loading and the magnitude of the Burgers vector of the partial dislocations. Figs. 9(a) and (b) show the effective SFE of the $\text{Co}_{60}\text{Ni}_{40}$ alloy and $\text{Co}_{20}\text{Cr}_{40}\text{Ni}_{40}$ MEA, respectively, at yield stress as a function of the TA orientation. Owing to the difference in yield strength (i.e., the difference in friction stress), the effective SFE in the $\text{Co}_{60}\text{Ni}_{40}$ alloy changed slightly, while the change in the $\text{Co}_{20}\text{Cr}_{40}\text{Ni}_{40}$ MEA was greater depending on the orientation. Even after yielding, where the leading and trailing partials start moving together, the difference in the effective SFE depending on the orientation can expand owing to the difference in the velocity of the partials [88,90]. This is because the velocity of dislocations increases with increasing resolved shear stress, which is proportional to the Schmid factor. This dynamical effect can be formulated as [88]

$$\gamma_{\text{Eff}} = \gamma_0 - \frac{m_{LP} - m_{TP}}{m_{LP} + m_{TP}} \sigma b_p. \quad (5)$$

Figs. 9(c) and (d) show the effective SFE of the $\text{Co}_{60}\text{Ni}_{40}$ alloy and $\text{Co}_{20}\text{Cr}_{40}\text{Ni}_{40}$ MEA, respectively, at the points exhibiting the maximum flow stress as a function of the TA orientation. Compared with the data in Figs. 9(a) and (b), the difference in the effective SFE distribution between the alloys expanded greatly. Owing to the higher flow stress (mainly due to the higher yield strength and high friction stress) in the $\text{Co}_{20}\text{Cr}_{40}\text{Ni}_{40}$ MEA, the variation in the effective SFE with grain orientation was much more severe than that in the $\text{Co}_{60}\text{Ni}_{40}$ alloy. These calculation results indicate that cross-slip of dislocations in the primary slip system is promoted in TA $\sim // \langle 1 \ 0 \ 0 \rangle$ oriented grains but inhibited in other grains. Although there is no guarantee that similar relationship holds for other slip systems activated in each grain of our polycrystalline specimens, this effect can contribute to the evolution of Type A and B microstructures observed in the $\text{Co}_{20}\text{Cr}_{40}\text{Ni}_{40}$ MEA and can explain the orientation dependence of the deformation microstructures observed in the $\text{Co}_{20}\text{Cr}_{40}\text{Ni}_{40}$ MEA as well as other high-alloy systems reported to date [9,10,11–18,29–37,91]. Above all, our results experimentally proved the validity of the model proposed by Copley and Kear [88] and by Kestenbach [89] through detailed and systematic comparisons between two model alloys with unified material properties and with low and high friction stress, which is closely related to the severe lattice distortion effect, one of the most important characteristics of

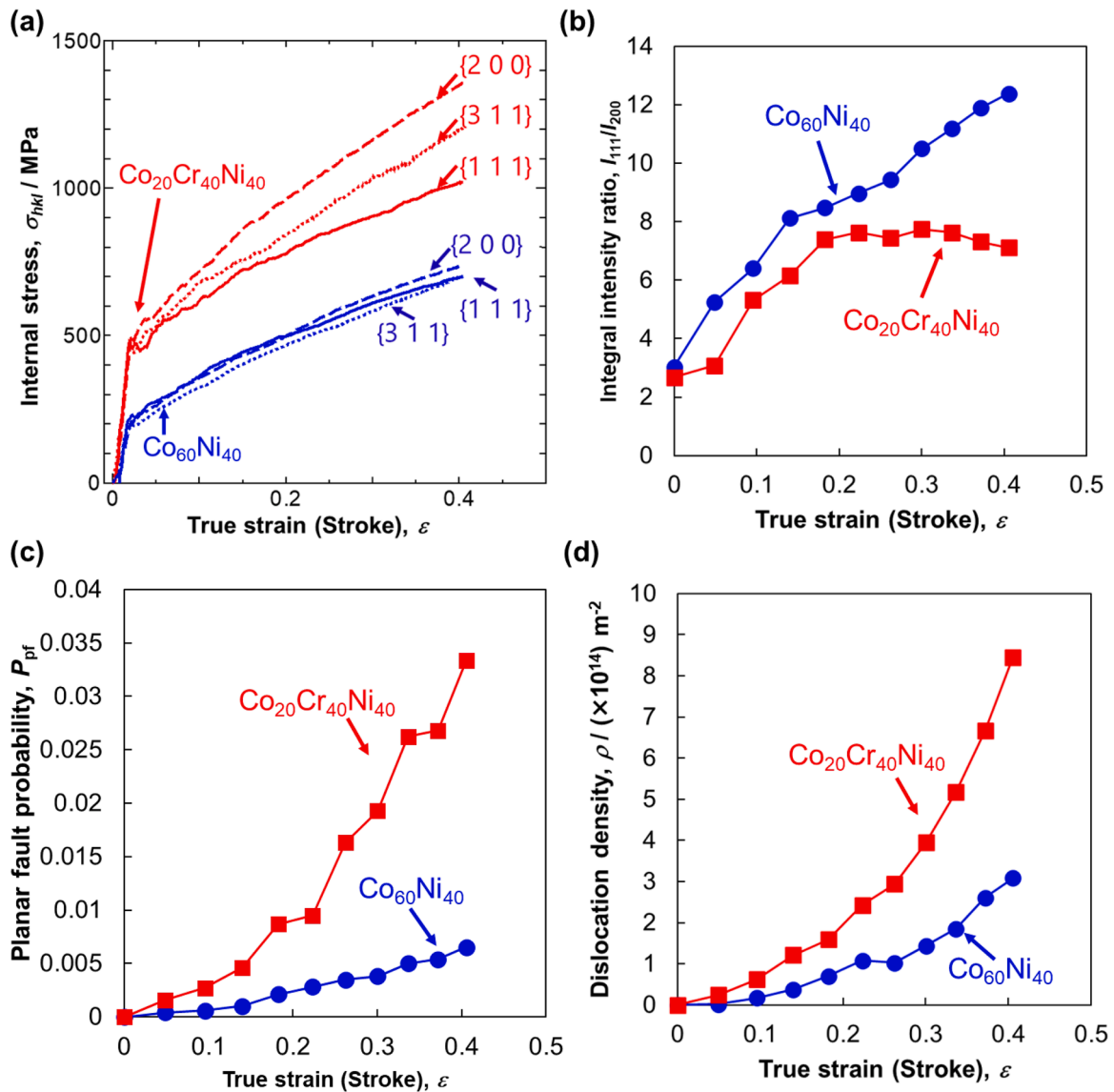


Fig. 7. (a) Internal stress in grains oriented to TA $\sim//$ (hkl) ($hkl = 111, 200$, and 311), (b) integral intensity ratio between 111 and 200 peaks, (c) planar fault probability, and (d) dislocation density calculated by the CMWP method as a function of applied true strain (calculated based on the stroke of the tensile test machine). The blue circles (and lines) and red squares (and lines) correspond to data for the $\text{Co}_{60}\text{Ni}_{40}$ alloy and $\text{Co}_{20}\text{Cr}_{40}\text{Ni}_{40}$ MEA. (For interpretation of the references to colour in this figure legend, the reader is referred to the web version of this article.)

HEAs/MEAs.

4.1.1.2. Chemical heterogeneity-induced variation of stacking fault width. Smith *et al.* [92] studied the core structure of dislocations in a CoCr-FeMnNi HEA using STEM and found that the local width of the stacking faults varied significantly more than that in conventional FCC dilute alloys and pure metals. Despite, they also employed atomistic simulations and showed that, with increasing the number and concentration of alloying elements, stacking faults became a wavy shape varying the width depending on the local chemical environment around each segment. Rao *et al.* [93] reported the same behavior in a $\text{Co}_{30}\text{Fe}_{16.67}\text{Ni}_{36.67}\text{Ti}_{16.67}$ alloy with an FCC structure by using molecular dynamics simulations. Their results suggest that the variation of stacking fault width could be prominent at room temperature as well as low temperature, and cross-slip of dislocations preferentially started from those sections having a smaller width. According to their description, only small segments of screw dislocations underwent cross-slip owing to low applied stress. These results suggest that cross-slip of screw dislocations can occur readily at positions with narrower stacking fault widths, while

simultaneously being restricted by wider sections. Therefore, complete cross-slip of screw dislocations may be difficult in high-alloy systems like the $\text{Co}_{20}\text{Cr}_{40}\text{Ni}_{40}$ MEA due to the existence of such wider parts in the stacking faults.

To correlate the above idea with the orientation dependence of deformation microstructure evolution in the materials, it is considered that one screw dislocation lying on the primary plane changes its slip plane by cross-slip. Fig. 10(a) shows ratio of the Schmid factor of the perfect dislocations belonging to the primary and cross-slip systems as a function of TA orientation. The stereographic triangle can be divided into two halves by the $21-1-011$ boundary. In grains having a positive (negative) Schmid factor ratio, cross-slip occurs preferentially with obtuse (acute) angles. Since cross-slip with acute angles is energetically and mechanically unfavorable, cross-slip (dynamic recovery) tends to be difficult in grains oriented to TA $\sim//$ $\langle 111 \rangle$ and easy in those oriented to TA $\sim//$ $\langle 100 \rangle$. Thus, the smaller DC size in the Type A-T grains (TA $\sim//$ $\langle 111 \rangle$) in the $\text{Co}_{60}\text{Ni}_{40}$ alloy can also be explained by the orientation dependence of the difficulty in cross-slip (inhibited dynamic recovery). In addition, if cross-slip is suppressed by the variation

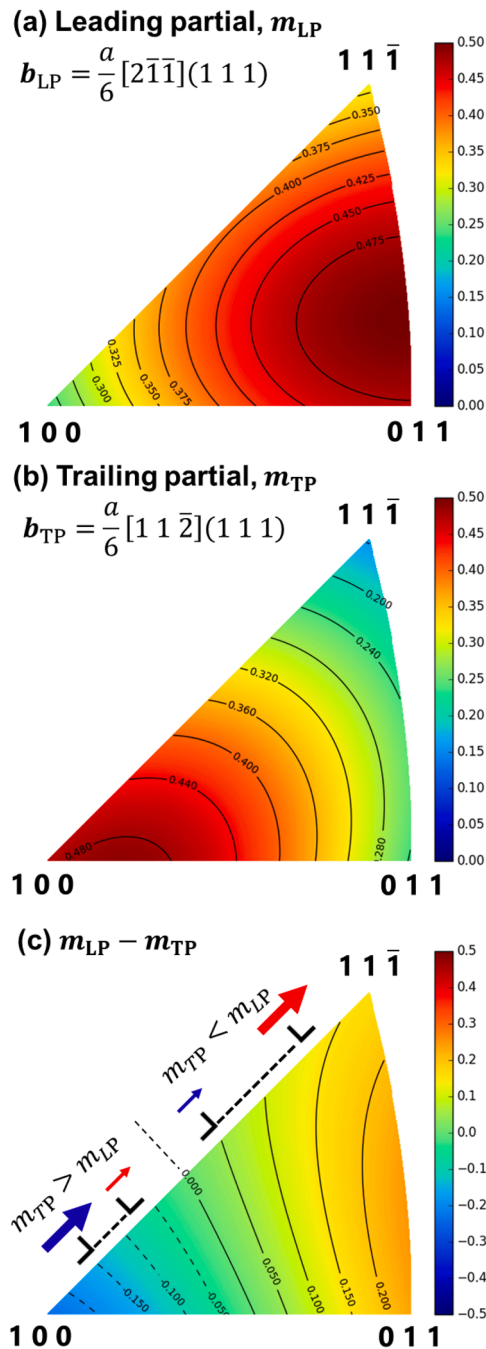


Fig. 8. Schmid factor of (a) leading (m_{LP}) and (b) trailing partial dislocations (m_{TP}) belonging to the primary slip system ($b = a/2 [1\ 0\ -1] (1\ 1\ 1)$) in FCC crystals as a function of TA orientation. (c) Difference between (a) and (b) ($m_{LP} - m_{TP}$). The color scales are provided in each figure.

of stacking fault width in the $\text{Co}_{20}\text{Cr}_{40}\text{Ni}_{40}$ MEA, the region where cross-slip is difficult in Fig. 10(a) may expand toward $\langle 1\ 0\ 0 \rangle$. This effect of chemical heterogeneity can also explain the orientation dependence of the deformation microstructure evolution in the $\text{Co}_{20}\text{Cr}_{40}\text{Ni}_{40}$ MEA. This effect could represent a unique mechanism in high-alloy systems, that is not significant in conventional FCC metals and alloys.

4.1.1.3. Element-element interaction (Solute-Solute interaction). As we proposed in our previous study [41], the element-element interaction, i. e., chemical interaction between each alloying element, which has been termed “solute-solute interaction” in conventional dilute systems, can play an important role in high-alloy systems. When dislocations glide

along slip planes, changes occur in the bonding combination of elements at the dislocation cores by shifting one atomic plane along the Burgers vector. Such local rearrangement of elements requires extra energy for dislocation motion in addition to the effect of atomic size misfit. This effect has recently been semi-quantitatively modeled by Nag *et al.* [94]. Theoretical studies by Nöhning and Curtin [95,96] showed that such solute-solute (element-element) interactions can increase activation energy for cross-slip of screw dislocations in FCC solid solutions. A similar idea has been proposed by Hong and Laird [97,98]. Therefore, the element-element interaction, which is one of the essential characteristics of HEAs/MEAs, can contribute to the suppression of cross-slip of screw dislocations in high-alloy systems. This mechanism can also expand the region where cross-slip is difficult in Fig. 10(a) toward $\langle 1\ 0\ 0 \rangle$. Thus, the orientation dependence of the deformation microstructure evolution in the $\text{Co}_{20}\text{Cr}_{40}\text{Ni}_{40}$ MEA can also be explained in the same manner as 4.1.1.2.

Although it is very challenging to theoretically or experimentally quantify the contribution of each effect, we think all these above-mentioned unique mechanisms can be responsible for the evolution of the characteristic deformation microstructures in the $\text{Co}_{20}\text{Cr}_{40}\text{Ni}_{40}$ MEA as well as other FCC high-alloy systems, depending on grain orientations.

4.1.2. Twinning behavior

In this study, we found that DTs were likely to be formed in grains oriented to TA $\sim // \langle 1\ 1\ 1 \rangle$, and the fraction of DTs in the $\text{Co}_{20}\text{Cr}_{40}\text{Ni}_{40}$ MEA was higher than that in the $\text{Co}_{60}\text{Ni}_{40}$ alloy. As DTs were formed along the plane with the highest Schmid factor (the primary plane), among various twinning models for FCC crystals [38,99,100], the Miura-Takamura-Narita (MTN) model [101,102] could explain the twinning behavior as follows. We assume that there are two slip systems (one of them is the primary slip system) intersecting each other and the Lomer-Cottrell immobile dislocation is formed (Fig. 10(b)). Since such immobile dislocations can be obstacles for dislocation motion, dislocations tend to pile-up against the immobile dislocations, and stress concentration occurs at the tip. In principle, there are two ways to relax the high stress at the tip: (i) cross-slip of dislocations, (ii) generating DTs along the primary plane. As explained in 4.1.1 above, cross-slip is generally unfavorable in grains oriented to TA $\sim // \langle 1\ 1\ 1 \rangle$, and DTs nucleate along the primary plane to relax the high stress, instead of cross-slip [102]. This is presumably why we observed DTs in grains oriented to TA $\sim // \langle 1\ 1\ 1 \rangle$ in the $\text{Co}_{60}\text{Ni}_{40}$ alloy, $\text{Co}_{20}\text{Cr}_{40}\text{Ni}_{40}$ MEA, and other FCC metals [103]. It should be noted that this mechanism can explain twin nucleation at grain boundaries in a consistent manner, as reported by Hong *et al.* [100]. Most importantly, in the cases of high-alloy systems like the $\text{Co}_{20}\text{Cr}_{40}\text{Ni}_{40}$ MEA, cross-slip is suppressed owing to the reasons discussed above (4.1.1.1-3). Accordingly, cross-slip in grains oriented to TA $\sim // \langle 1\ 1\ 1 \rangle$ can be much more difficult in high-alloy systems than conventional systems including the $\text{Co}_{60}\text{Ni}_{40}$ alloy. Thus, DTs progressively nucleated more in the $\text{Co}_{20}\text{Cr}_{40}\text{Ni}_{40}$ MEA than in the $\text{Co}_{60}\text{Ni}_{40}$ alloy.

4.2. Characteristics of deformation mechanisms in FCC high-alloy systems

As explained in the previous section, the cross-slip of screw dislocations in the $\text{Co}_{20}\text{Cr}_{40}\text{Ni}_{40}$ MEA is more suppressed than in the $\text{Co}_{60}\text{Ni}_{40}$ alloy, resulting in the formation of PDS, fine DCs, and DTs. Compared with the $\text{Co}_{60}\text{Ni}_{40}$ alloy, which exhibits mainly coarse DCs, the characteristic deformation microstructure evolution in the $\text{Co}_{20}\text{Cr}_{40}\text{Ni}_{40}$ MEA is advantageous in terms of achieving superior mechanical properties as follows.

4.2.1. Dislocation density evolution

Since cross-slip is suppressed in the $\text{Co}_{20}\text{Cr}_{40}\text{Ni}_{40}$ MEA, dynamic recovery during deformation is presumably inhibited. In addition, as we

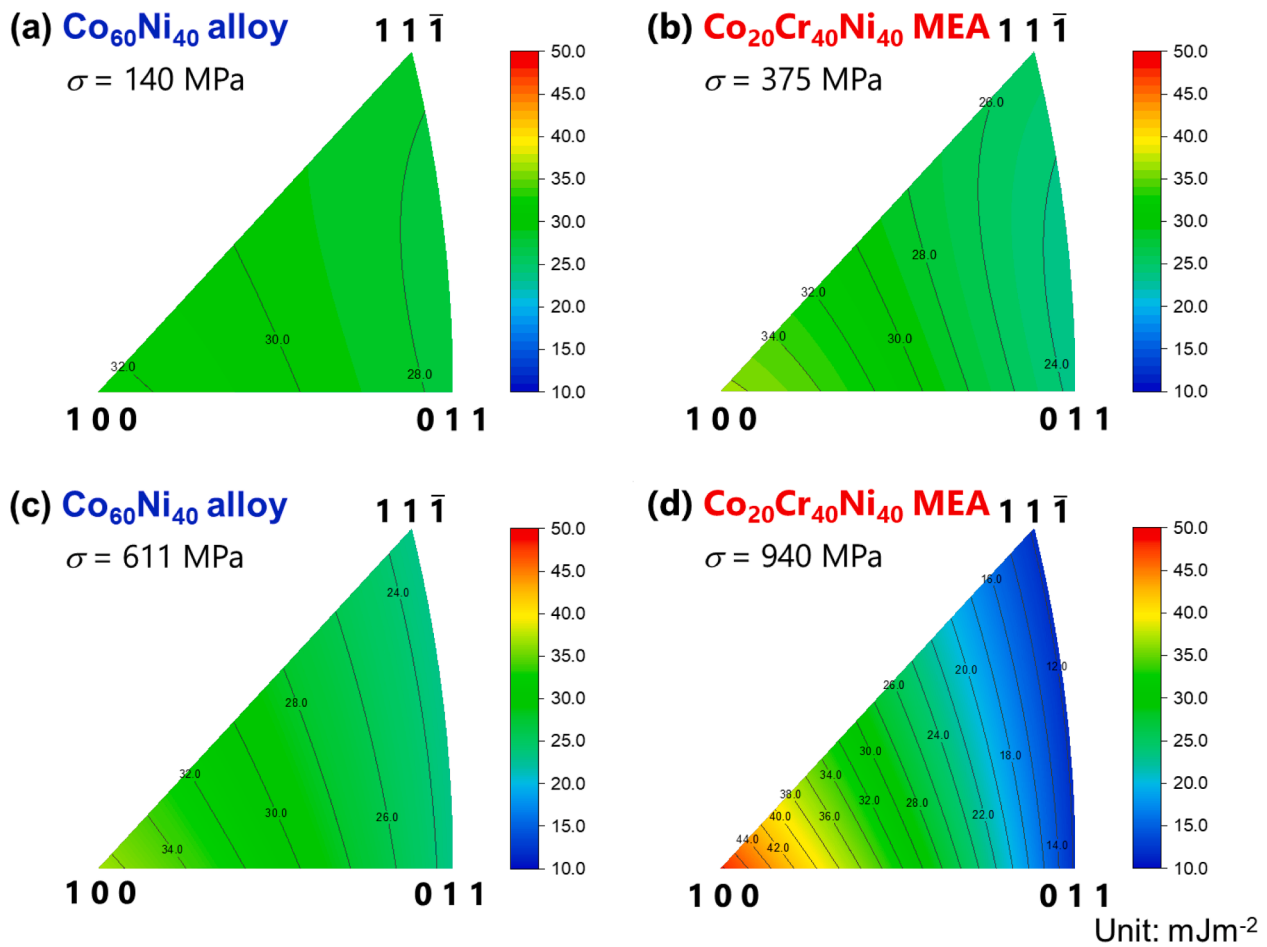


Fig. 9. Effective SFE of (a) the $\text{Co}_{60}\text{Ni}_{40}$ alloy and (b) $\text{Co}_{20}\text{Cr}_{40}\text{Ni}_{40}$ MEA at yield point (the corresponding true flow stresses are indicated in the figure) as a function of TA orientation, calculated by eq. (4). Effective SFE of (c) the $\text{Co}_{60}\text{Ni}_{40}$ alloy and (d) $\text{Co}_{20}\text{Cr}_{40}\text{Ni}_{40}$ MEA at the maximum flow stress point (the corresponding true flow stresses are indicated in the figure) as a function of TA, calculated by eq. (5), considering the dynamical effect. The color scales are provided in each figure.

observed by ET (Section 3.4), stair-rod immobile dislocations can be easily formed in the $\text{Co}_{20}\text{Cr}_{40}\text{Ni}_{40}$ MEA because of the suppressed cross-slip. The formation of immobile dislocations generally promotes dislocation multiplication as dislocations cut each other, making new dislocation sources [82].

Fig. 11 plots the tensile flow stress (true stress) of the materials as a function of the square root of dislocation density (ρ), as measured by the in-situ XRD (Section 3.5). The linear relationship is the so-called Bailey-Hirsch relationship [45], expressed as

$$\sigma = \sigma_Y + \alpha M G b \sqrt{\rho}, \quad (6)$$

where σ_Y is the yield strength, α is a constant, M is the Taylor factor (assumed to be 3.06 for a random texture), and G is the shear modulus. By fitting the data in Fig. 11 by eq. (6), we obtained α values of 0.341 and 0.371 for the $\text{Co}_{20}\text{Cr}_{40}\text{Ni}_{40}$ MEA and the $\text{Co}_{60}\text{Ni}_{40}$ alloy, respectively. This is in good agreement with the values reported to date for other FCC materials, ranging from about 0.3 to 0.5 [45]. This result indicates that the evolution of dislocation densities played a major role in the work-hardening of the materials. Thus, we believe that the high dislocation density was the main reason for the high work-hardening ability of the $\text{Co}_{20}\text{Cr}_{40}\text{Ni}_{40}$ MEA.

4.2.2. Grain refinement by deformation twins

The shear deformation induced by DTs is much smaller in FCC metals than in materials with other crystal structures like HCP metals [99]. Rather, in FCC metals, twin boundaries act as obstacles for dislocation motion, similarly to ordinary grain boundaries [104]. Also, dislocation

density near the boundaries can locally increase to maintain the deformation compatibility with neighboring grains with different crystal orientations (This effect can be included in 4.2.1 above). As a result, a higher work-hardening ability can be obtained (the so-called dynamic Hall-Petch effect [38]). As shown in Figs. 3 and 4, the fraction of DTs in the $\text{Co}_{20}\text{Cr}_{40}\text{Ni}_{40}$ MEA was much higher than in the $\text{Co}_{60}\text{Ni}_{40}$ alloy owing to the suppressed cross-slip. Although the proportion of grains having DTs was less than 10% in the MEA, the formation of a high density of DTs could also have partly contributed to the higher work-hardening ability.

5. Conclusion

We compared the mechanical properties of the $\text{Co}_{60}\text{Ni}_{40}$ alloy (with low friction stress) and $\text{Co}_{20}\text{Cr}_{40}\text{Ni}_{40}$ MEA (with high friction stress) having similar material properties such as SFE and elastic constants and investigated the deformation microstructure evolution during tensile deformation by a conventional TEM and three-dimensional ET techniques as well as in-situ XRD. We obtained the following results:

- (1) Tensile tests were performed at room temperature. The $\text{Co}_{20}\text{Cr}_{40}\text{Ni}_{40}$ MEA was found to show a higher yield strength and a higher work-hardening rate than the $\text{Co}_{60}\text{Ni}_{40}$ alloy, resulting in a superior strength-ductility balance in the MEA.
- (2) In the $\text{Co}_{60}\text{Ni}_{40}$ alloy, most grains developed coarse DCs regardless of the grain orientation. A few grains oriented to TA $\sim // \langle 111 \rangle$ showed a small number of DTs.

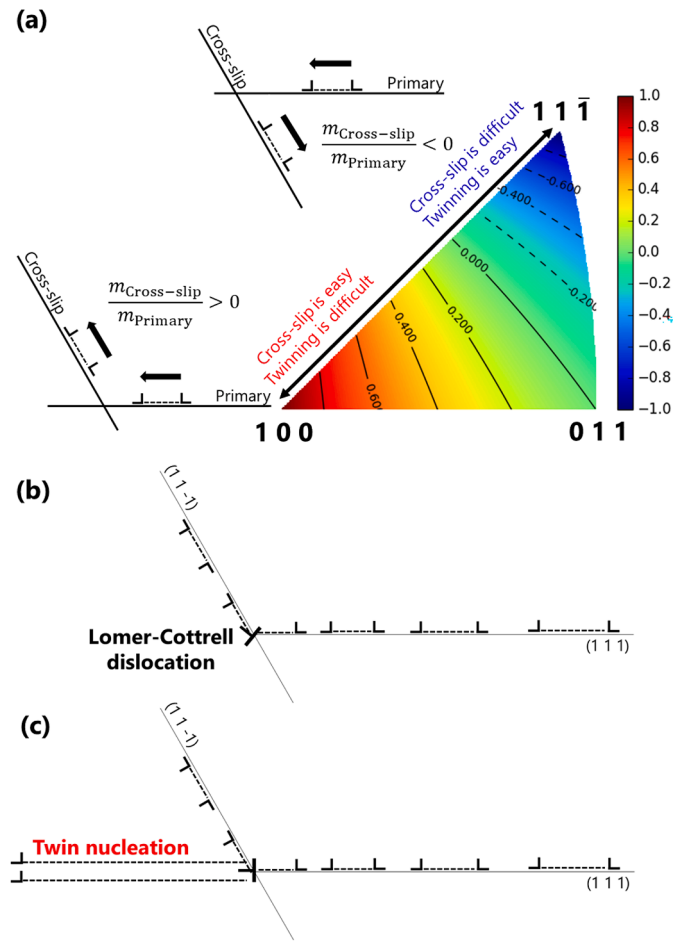


Fig. 10. The ratio between the Schmid factors in the primary (m_{Primary}) and cross-slip systems ($m_{\text{Cross-slip}}$) as a function of TA orientation. Schematics showing (b) formation of a Lomer-Cottrell dislocation at the intersection of two slip planes and (c) nucleation of a DT along the primary plane, according to the MTN model.

- (3) In the $\text{Co}_{20}\text{Cr}_{40}\text{Ni}_{40}$ MEA, fine DCs were observed in grains oriented to TA $\sim // \langle 100 \rangle$, while PDS were observed in others. Many DTs were formed in grains oriented to TA $\sim // \langle 111 \rangle$.
- (4) Three-dimensional structure of the PDS in the $\text{Co}_{20}\text{Cr}_{40}\text{Ni}_{40}$ MEA at the initial stage of deformation was resolved by ET. Many of the dislocations were confined to specific $\{111\}$ planes. Dislocations belonging to two different slip systems were found to intersect each other, leaving stair-rod immobile dislocations.
- (5) In-situ XRD measurements during tensile deformation revealed different trends in internal stress and texture development for the $\text{Co}_{60}\text{Ni}_{40}$ alloy and $\text{Co}_{20}\text{Cr}_{40}\text{Ni}_{40}$ MEA, suggesting a heterogeneous deformation microstructure evolution in the MEA. The increase in both planar fault probability and dislocation density during deformation was much larger in the MEA than in the $\text{Co}_{60}\text{Ni}_{40}$ alloy.
- (6) The correlation between the evolution of the characteristic deformation microstructures and the macroscopic mechanical properties (work-hardening behavior) in the MEA was clarified in detail through combining the results of two-/three-dimensional TEM characterization of deformation microstructures and the quantitative evaluation of dislocation density and planar fault probability by in-situ synchrotron XRD.

In brief, our results imply that cross-slip of screw dislocations and dynamic recovery in FCC high-alloy systems (e.g., HEAs, MEAs, and

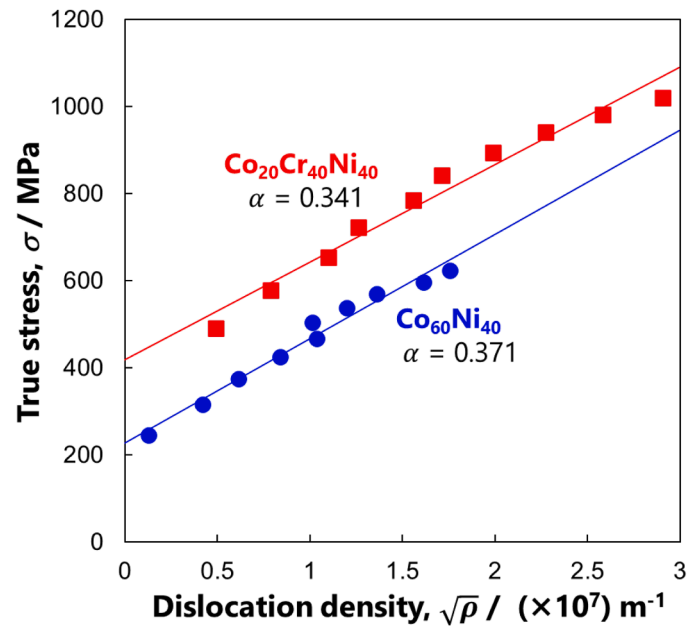


Fig. 11. The relationship between the tensile flow stress (true stress) and the square root of dislocation density measured by the in-situ XRD (Fig. 7(d)). The blue circles (and line) and red squares (and line) correspond to the data for the $\text{Co}_{60}\text{Ni}_{40}$ alloy and $\text{Co}_{20}\text{Cr}_{40}\text{Ni}_{40}$ MEA, respectively. The solid lines were fitted by the Bailey-Hirsch relationship (eq. (6)), and the α values obtained for both materials are given in the figure. (For interpretation of the references to colour in this figure legend, the reader is referred to the web version of this article.)

austenitic steels) are inhibited by (i) stress-induced, (ii) chemical heterogeneity-induced variation of stacking fault width, and (iii) element-element interaction, leading to a characteristic deformation microstructure evolution and enhanced work-hardening mainly due to high dislocation density as well as planar faults density. This means that FCC high-alloy systems inherently exhibit superior mechanical properties because of the effect of alloying multiple elements with high concentrations (not simply because SFE decreases). We believe that the present findings will pave the way to new design principles for structural materials that overcome the dilemma of strength-ductility trade-off in conventional metallic materials.

CRediT authorship contribution statement

Shuhei Yoshida: Writing – original draft, Visualization, Validation, Methodology, Investigation, Funding acquisition, Formal analysis, Data curation, Conceptualization. **Rui Fu:** Visualization, Software, Methodology, Investigation, Formal analysis, Data curation. **Wu Gong:** Writing – review & editing, Formal analysis. **Takuto Ikeuchi:** Writing – review & editing, Investigation, Data curation. **Yu Bai:** Writing – review & editing, Supervision. **Zongqiang Feng:** Writing – review & editing, Visualization, Supervision, Resources, Methodology, Funding acquisition, Formal analysis. **Guilin Wu:** Writing – review & editing, Visualization, Supervision, Methodology, Funding acquisition. **Akinobu Shibata:** Writing – review & editing, Supervision. **Niels Hansen:** Writing – review & editing, Supervision. **Xiaoxu Huang:** Writing – review & editing, Supervision, Resources, Project administration, Funding acquisition, Conceptualization. **Nobuhiro Tsuji:** Writing – review & editing, Supervision, Resources, Project administration, Funding acquisition, Conceptualization.

Declaration of competing interest

The authors declare that they have no known competing financial interests or personal relationships that could have appeared to influence

the work reported in this paper.

Acknowledgments

This work was financially supported by the Elements Strategy Initiative for Structural Materials (ESISM, No. JPMXP0112101000), Japan Society for the Promotion of Science (JSPS) the Fund for the Promotion of Joint International Research (International Leading Research) (No. JP23K20037), the Grant-in-Aid for Scientific Research on Innovative Area "High Entropy Alloys" (No. JP18H05455), the Grant-in-Aid for Scientific Research (A) (Nos. JP20H00306, and JP23H00234), the Grant-in-Aid for Early-Career Scientists (No. JP22K14501), the Grant-in-Aid for Research Activity Start-up (No. JP21K20487), and the Grant-in-Aid for JSPS Research Fellow (No. JP18J20766), all through the Ministry of Education, Culture, Sports, Science and Technology (MEXT), Japan. SY also acknowledges the financial support of Mazume research encouragement prize, Graduate School of Engineering, Kyoto University. RF, ZQF, and XH acknowledge supports from the National Natural Science Foundation of China (Nos. 51971045 and 52071038). The synchrotron X-ray diffraction experiments were performed at the BL46XU of SPring-8 with the approval of the Japan Synchrotron Radiation Research Institute (JASRI) (Proposal No. 2019B1801). All the supports are greatly appreciated.

The authors thank Dr. Tianbo Yu and Ms. Gitte Christiansen of Technical University of Denmark (Denmark), Prof. Mitsuhiro Murayama of Virginia Polytechnic Institute and State University (USA), and Mr. Akira Yasuhara of JEOL Ltd. (Japan) for the technical advice on the transmission electron microscopy experiments. The authors also thank Dr. Masugu Sato of JASRI (Japan) and Prof. Hiroki Adachi of the University of Hyogo (Japan) for their technical assistance on the synchrotron radiation experiments. The authors note that this work is a part (Chapter 3) of the doctoral dissertation of SY.

Supplementary materials

Supplementary material associated with this article can be found, in the online version, at [doi:10.1016/j.actamat.2024.120498](https://doi.org/10.1016/j.actamat.2024.120498).

References

- [1] X. Huang, N. Hansen, Grain orientation dependence of microstructure in aluminium deformed in tension, *Scr. Mater.* 37 (1997) 1–7, [https://doi.org/10.1016/S1359-6462\(97\)00072-9](https://doi.org/10.1016/S1359-6462(97)00072-9).
- [2] X. Huang, Grain orientation effect on microstructure in tensile strained copper, *Scr. Mater.* 38 (1998) 1697–1703, [https://doi.org/10.1016/S1359-6462\(98\)00051-7](https://doi.org/10.1016/S1359-6462(98)00051-7).
- [3] X. Huang, G. Winther, Dislocation structures. Part I. Grain orientation dependence, *Philos. Mag.* 87 (2007) 5189–5214, <https://doi.org/10.1080/14786430701652851>.
- [4] N. Hansen, R.F. Mehl, New discoveries in deformed metals, *Metall. Mater. Trans. A Phys. Metall. Mater. Sci.* 32 (2001) 2917–2935, <https://doi.org/10.1007/s11661-001-0167-x>.
- [5] N. Hansen, X. Huang, W. Pantleon, G. Winther, Grain orientation and dislocation patterns, *Philos. Mag.* 86 (2006) 3981–3994, <https://doi.org/10.1080/14786430600654446>.
- [6] G. Winther, X. Huang, Dislocation structures. Part II. Slip system dependence, *Philos. Mag.* 87 (2007) 5215–5235, <https://doi.org/10.1080/14786430701591505>.
- [7] G.M. Le, A. Godfrey, N. Hansen, W. Liu, G. Winther, X. Huang, Influence of grain size in the near-micrometre regime on the deformation microstructure in aluminium, *Acta Mater.* 61 (2013) 7072–7086, <https://doi.org/10.1016/j.actamat.2013.07.046>.
- [8] D.A. Hughes, N. Hansen, The microstructural origin of work hardening stages, *Acta Mater.* 148 (2018) 374–383, <https://doi.org/10.1016/j.actamat.2018.02.002>.
- [9] I. Gutierrez-Urrutia, D. Raabe, Grain size effect on strain hardening in twinning-induced plasticity steels, *Scr. Mater.* 66 (2012) 992–996, <https://doi.org/10.1016/j.scriptamat.2012.01.037>.
- [10] I. Gutierrez-Urrutia, D. Raabe, Multistage strain hardening through dislocation substructure and twinning in a high strength and ductile weight-reduced Fe–Mn–Al–C steel, *Acta Mater.* 60 (2012) 5791–5802, <https://doi.org/10.1016/j.actamat.2012.07.018>.
- [11] I. Karaman, H. Sehitoglu, K. Gall, Y.I. Chumlyakov, On the deformation mechanisms in single crystal hadfield manganese steels, *Scr. Mater.* 38 (1998) 1009–1015, [https://doi.org/10.1016/S1359-6462\(97\)00581-2](https://doi.org/10.1016/S1359-6462(97)00581-2).
- [12] I. Karaman, H. Sehitoglu, K. Gall, Y... Chumlyakov, H... Maier, Deformation of single crystal Hadfield steel by twinning and slip, *Acta Mater.* 48 (2000) 1345–1359, [https://doi.org/10.1016/S1359-6454\(99\)00383-3](https://doi.org/10.1016/S1359-6454(99)00383-3).
- [13] E.G. Zakharova, I.V. Kireeva, Y.I. Chumlyakov, S.P. Efimenko, H. Sehitoglu, I. Karaman, Deformation mechanisms and strain hardening of Hadfield-steel single crystals alloyed with aluminum, *Dokl. Phys.* 47 (2002) 515–517, <https://doi.org/10.1134/1.1499189>.
- [14] D. Canadinc, I. Karaman, H. Sehitoglu, Y.I. Chumlyakov, H.J. Maier, The role of nitrogen on the deformation response of hadfield steel single crystals, *Metall. Mater. Trans. A Phys. Metall. Mater. Sci.* 34 A (2003) 1821–1831, <https://doi.org/10.1007/s11661-003-0148-3>.
- [15] P. Müllner, C. Solenthaler, P. Uggowitzer, M.O.O. Speidel, On the Effect of Nitrogen On the Dislocation Structure of Austenitic Stainless Steel, *Elsevier*, 1993.
- [16] Y.I. Chumlyakov, I.V. Kireeva, A.D. Korotaev, E.I. Litvinova, Y.L. Zuev, Mechanisms of plastic deformation, hardening, and fracture in single crystals of nitrogen-containing austenitic stainless steels, *Russ. Phys. J.* 39 (1996) 189–210, <https://doi.org/10.1007/BF02067642>.
- [17] I. Karaman, H. Sehitoglu, H.J. Maier, Y.I. Chumlyakov, Competing mechanisms and modeling of deformation in austenitic stainless steel single crystals with and without nitrogen, *Acta Mater.* 49 (2001) 3919–3933, [https://doi.org/10.1016/S1359-6454\(01\)00296-8](https://doi.org/10.1016/S1359-6454(01)00296-8).
- [18] I. Karaman, H. Sehitoglu, Y.I. Chumlyakov, H.J. Maier, The deformation of low-stacking-fault-energy austenitic steels, *JOM* 54 (2002) 31–37, <https://doi.org/10.1007/BF02700983>.
- [19] R. Uejii, N. Tsuchida, D. Terada, N. Tsuji, Y. Tanaka, A. Takemura, K. Kunishige, Tensile properties and twinning behavior of high manganese austenitic steel with fine-grained structure, *Scr. Mater.* 59 (2008) 963–966, <https://doi.org/10.1016/j.scriptamat.2008.06.050>.
- [20] B. Cantor, I.T.H. Chang, P. Knight, A.J.B. Vincent, Microstructural development in equiatomic multicomponent alloys, *Mater. Sci. Eng. A.* 375–377 (2004) 213–218, <https://doi.org/10.1016/j.msea.2003.10.257>.
- [21] J.-W. Yeh, S.-K. Chen, S.-J. Lin, J.-Y. Gan, T.-S. Chin, T.-T. Shun, C.-H. Tsau, S.-Y. Chang, Nanostructured high-entropy alloys with multiple principal elements: novel alloy design concepts and outcomes, *Adv. Eng. Mater.* 6 (2004) 299–303, <https://doi.org/10.1002/adem.200300567>.
- [22] M.-H. Tsai, J.-W. Yeh, High-entropy alloys: a critical review, *Mater. Res. Lett.* 2 (2014) 107–123, <https://doi.org/10.1080/21663831.2014.912690>.
- [23] D.B. Miracle, O.N. Senkov, A critical review of high entropy alloys and related concepts, *Acta Mater.* 122 (2017) 448–511, <https://doi.org/10.1016/j.actamat.2016.08.081>.
- [24] E.P. George, D. Raabe, R.O. Ritchie, High-entropy alloys, *Nat. Rev. Mater.* 4 (2019) 515–534, <https://doi.org/10.1038/s41578-019-0121-4>.
- [25] H. Inui, K. Kishida, Z. Chen, Recent progress in our understanding of phase stability, atomic structures and mechanical and functional properties of high-entropy alloys, *Mater. Trans.* 63 (2022), <https://doi.org/10.2320/matertrans.MT-M2021234>.
- [26] G. Laplanche, A. Kostka, O.M. Horst, G. Eggeler, E.P. George, Microstructure evolution and critical stress for twinning in the CrMnFeCoNi high-entropy alloy, *Acta Mater.* 118 (2016) 152–163, <https://doi.org/10.1016/j.actamat.2016.07.038>.
- [27] G. Laplanche, A. Kostka, C. Reinhart, J. Hunfeld, G. Eggeler, E.P. George, Reasons for the superior mechanical properties of medium-entropy CrCoNi compared to high-entropy CrMnFeCoNi, *Acta Mater.* 128 (2017) 292–303, <https://doi.org/10.1016/j.actamat.2017.02.036>.
- [28] D. Xu, M. Wang, T. Li, X. Wei, Y. Lu, A critical review of the mechanical properties of CoCrNi-based medium-entropy alloys, *Microstruct.* 2 (2022) (2022), <https://doi.org/10.20517/MICROSTRUCTURES.2021.10.22022001N/A-N/A>.
- [29] I.V. Kireeva, Y.I. Chumlyakov, Z.V. Pobedennaya, Y.N. Platonova, I. V. Kuksgauzen, D.A. Kuksgauzen, V.V. Poklonov, I. Karaman, H. Sehitoglu, Slip and twinning in the [1̄ 49]-oriented single crystals of a high-entropy alloy, *Russ. Phys. J.* 59 (2016) 1242–1250, <https://doi.org/10.1007/s11182-016-0898-1>.
- [30] W. Abuzaid, H. Sehitoglu, Critical resolved shear stress for slip and twin nucleation in single crystalline FeNiCoCrMn high entropy alloy, *Mater. Charact.* 129 (2017) 288–299, <https://doi.org/10.1016/j.matchar.2017.05.014>.
- [31] I.V. Kireeva, Y.I. Chumlyakov, Z.V. Pobedennaya, I.V. Kuksgauzen, I. Karaman, Orientation dependence of twinning in single crystalline CoCrFeMnNi high-entropy alloy, *Mater. Sci. Eng. A.* 705 (2017) 176–181, <https://doi.org/10.1016/j.msea.2017.08.065>.
- [32] I.V. Kireeva, Y.I. Chumlyakov, Z.V. Pobedennaya, A.V. Vyrodova, I. Karaman, Twinning in [001]-oriented single crystals of CoCrFeMnNi high-entropy alloy at tensile deformation, *Mater. Sci. Eng. A.* 713 (2018) 253–259, <https://doi.org/10.1016/j.msea.2017.12.059>.
- [33] I.V. Kireeva, Y.I. Chumlyakov, Z.V. Pobedennaya, A.V. Vyrodova, I. V. Kuksgauzen, D.A. Kuksgauzen, Orientation and temperature dependence of a planar slip and twinning in single crystals of Al0.3CoCrFeNi high-entropy alloy, *Mater. Sci. Eng. A.* 737 (2018) 47–60, <https://doi.org/10.1016/j.msea.2018.09.025>.
- [34] M. Bönsch, Y. Wu, H. Sehitoglu, Hardening by slip-twin and twin-twin interactions in FeMnNiCoCr, *Acta Mater.* 153 (2018) 391–403, <https://doi.org/10.1016/j.actamat.2018.04.054>.
- [35] B. Uzer, S. Picak, J. Liu, T. Jozaghi, D. Canadinc, I. Karaman, Y.I. Chumlyakov, I. Kireeva, On the mechanical response and microstructure evolution of NiCoCr

- single crystalline medium entropy alloys, *Mater. Res. Lett.* 6 (2018) 442–449, <https://doi.org/10.1080/21663831.2018.1478331>.
- [36] I.V. Kireeva, Y.I. Chumlyakov, A.V. Vyrodova, Z.V. Pobedennaya, I. Karaman, Effect of twinning on the orientation dependence of mechanical behaviour and fracture in single crystals of the equiatomic CoCrFeMnNi high-entropy alloy at 77K, *Mater. Sci. Eng. A*. 784 (2020) 139315, <https://doi.org/10.1016/j.msea.2020.139315>.
- [37] W. Abuzaid, L. Patriarca, A study on slip activation for a coarse-grained and single crystalline CoCrNi medium entropy alloy, *Intermetallics* 117 (2020) 106682, <https://doi.org/10.1016/j.intermet.2019.106682>.
- [38] B.C. De Cooman, Y. Estrin, S.K. Kim, Twinning-induced plasticity (TWIP) steels, *Acta Mater.* 142 (2018) 283–362, <https://doi.org/10.1016/j.actamat.2017.06.046>.
- [39] V. Gerold, H.P. Karnthaler, On the origin of planar slip in f.c.c. alloys, *Acta Metall* 37 (1989) 2177–2183, [https://doi.org/10.1016/0001-6160\(89\)90143-0](https://doi.org/10.1016/0001-6160(89)90143-0).
- [40] S. Yoshida, T. Bhattacharjee, Y. Bai, N. Tsuji, Friction stress and Hall-Petch relationship in CoCrNi equi-atomic medium entropy alloy processed by severe plastic deformation and subsequent annealing, *Scr. Mater.* 134 (2017) 33–36, <https://doi.org/10.1016/j.scriptamat.2017.02.042>.
- [41] S. Yoshida, T. Ikeuchi, T. Bhattacharjee, Y. Bai, A. Shibata, N. Tsuji, Effect of elemental combination on friction stress and Hall-Petch relationship in face-centered cubic high /medium entropy alloys, *Acta Mater.* 171 (2019) 201–215, <https://doi.org/10.1016/j.actamat.2019.04.017>.
- [42] B. Yin, S. Yoshida, N. Tsuji, W.A. Curtin, Yield strength and misfit volumes of NiCoCr and implications for short-range-order, *Nat. Commun.* 11 (2020) 2507, <https://doi.org/10.1038/s41467-020-16083-1>.
- [43] R. Labusch, A statistical theory of solid solution hardening, *Phys. Status Solidi.* 41 (1970) 659–669.
- [44] R. Labusch, Statistische theorien der mischkristallhärtung, *Acta Metall.* 20 (1972) 917–927, [https://doi.org/10.1016/0001-6160\(72\)90085-5](https://doi.org/10.1016/0001-6160(72)90085-5).
- [45] A.S. Argon, *Strengthening Mechanisms in Crystal Plasticity*, Oxford University Press, Oxford, UK, 2008.
- [46] G.P.M. Leyson, W.A. Curtin, L.G. Hector, C.F. Woodward, Quantitative prediction of solute strengthening in aluminium alloys, *Nat. Mater.* 9 (2010) 750–755, <https://doi.org/10.1038/nmat2813>.
- [47] C. Varvenne, A. Luque, W.A. Curtin, Theory of strengthening in fcc high entropy alloys, *Acta Mater* 118 (2016) 164–176, <https://doi.org/10.1016/j.actamat.2016.07.040>.
- [48] C. Varvenne, G.P.M. Leyson, M. Ghazisaeidi, W.A. Curtin, Solute strengthening in random alloys, *Acta Mater.* 124 (2017) 660–683, <https://doi.org/10.1016/j.actamat.2016.09.046>.
- [49] M. Considère, L'emploi du fer de l'acier dans les constructions, *Memoire no 34, Ann. Des. Ponts Chaussées* 9 (1885) 574–775.
- [50] S.J. Sun, Y.Z. Tian, H.R. Lin, X.G. Dong, Y.H. Wang, Z.J. Wang, Z.F. Zhang, Temperature dependence of the Hall–Petch relationship in CoCrFeMnNi high-entropy alloy, *J. Alloys Compd.* 806 (2019) 992–998, <https://doi.org/10.1016/j.jallcom.2019.07.357>.
- [51] Z. Wu, H. Bei, G.M. Pharr, E.P. George, Temperature dependence of the mechanical properties of equiatomic solid solution alloys with face-centered cubic crystal structures, *Acta Mater* 81 (2014) 428–441, <https://doi.org/10.1016/j.actamat.2014.08.026>.
- [52] S. Yoshida, R. Fu, W. Gong, T. Ikeuchi, Y. Bai, Z. Feng, G. Wu, A. Shibata, N. Hansen, X. Huang, N. Tsuji, Grain orientation dependence of deformation microstructure evolution and mechanical properties in face-centered cubic high/medium entropy alloys, *IOP Conf. Ser. Mater. Sci. Eng.* 1249 (2022) 012027, <https://doi.org/10.1088/1757-899X/1249/1/012027>.
- [53] B.E.P.P. Beeston, I.L. Dillamore, R.E. Smallman, The stacking-fault energy of some Nickel-Cobalt alloys, *Met. Sci. J.* 2 (1968) 12–14, <https://doi.org/10.1179/030634568790443468>.
- [54] E.H. Köster, A.R. Thölen, A. Howie, Stacking fault energies of Ni–Co–Cr alloys, *Philos. Mag.* 10 (1964) 1093–1095, <https://doi.org/10.1080/14786436408225417>.
- [55] S. Yoshida, T. Ikeuchi, Y. Bai, A. Shibata, N. Hansen, X. Huang, N. Tsuji, Deformation microstructures and strength of face-centered cubic high/medium entropy alloys, *IOP Conf. Ser. Mater. Sci. Eng.* 580 (2019) 012053.
- [56] S. Yoshida, T. Ikeuchi, Y. Bai, N. Tsuji, Effect of cobalt-content on mechanical properties of non-equiatOmic Co–Cr–Ni medium entropy alloys, *Mater. Trans.* 61 (2020) 587–595, <https://doi.org/10.2320/matertrans.MT-MK2019004>.
- [57] H. Schreier, J.J. Orteu, M.A. Sutton, *Image Correlation For shape, Motion and Deformation measurements: Basic concepts, Theory and Applications*, Springer US, Boston, 2009, <https://doi.org/10.1007/978-0-387-78747-3>.
- [58] P.J. Phillips, M.J. Mills, M. De Graef, Systematic row and zone axis STEM defect image simulations, *Philos. Mag.* 91 (2011) 2081–2101, <https://doi.org/10.1080/14786435.2010.547526>.
- [59] P.J. Phillips, M.C. Brandes, M.J. Mills, M. de Graef, Diffraction contrast STEM of dislocations: imaging and simulations, *Ultramicroscopy* 111 (2011) 1483–1487, <https://doi.org/10.1016/j.ultramic.2011.07.001>.
- [60] Y. Zhu, C. Ophus, M.B. Toloczko, D.J. Edwards, Towards bend-contour-free dislocation imaging via diffraction contrast STEM, *Ultramicroscopy* 193 (2018) 12–23, <https://doi.org/10.1016/j.ultramic.2018.06.001>.
- [61] Q. Liu, A simple and rapid method for determining orientations and misorientations of crystalline specimens in TEM, *Ultramicroscopy* 60 (1995) 81–89, [https://doi.org/10.1016/0304-3991\(95\)00049-7](https://doi.org/10.1016/0304-3991(95)00049-7).
- [62] S. Zaefferer, New developments of computer-aided crystallographic analysis in transmission electron microscopy, *J. Appl. Crystallogr.* 33 (2000) 10–25, <https://doi.org/10.1107/S0021889899010894>.
- [63] J.S. Barnard, J. Sharp, J.R. Tong, P.A. Midgley, High-resolution three-dimensional imaging of dislocations, *Science (80-)* 313 (2006) 319, <https://doi.org/10.1126/science.1125783>.
- [64] G.S. Liu, S.D. House, J. Kacher, M. Tanaka, K. Higashida, I.M. Robertson, Electron tomography of dislocation structures, *Mater. Charact.* 87 (2014) 1–11, <https://doi.org/10.1016/j.matchar.2013.09.016>.
- [65] Z. Feng, R. Fu, C. Lin, G. Wu, T. Huang, L. Zhang, X. Huang, TEM-based dislocation tomography: challenges and opportunities, *Curr. Opin. Solid State Mater. Sci.* (2020) 100833, <https://doi.org/10.1016/j.cossms.2020.100833>.
- [66] S. Hata, T. Honda, H. Saito, M. Mitsuhashi, T.C. Petersen, M. Murayama, Electron tomography: an imaging method for materials deformation dynamics, *Curr. Opin. Solid State Mater. Sci.* (2020) 100850, <https://doi.org/10.1016/j.cossms.2020.100850>.
- [67] M. Radermacher, Weighted back-projection methods, *Electron Tomogr* (1992) 91–115, https://doi.org/10.1007/978-1-4757-2163-8_5.
- [68] G. Ribárik, *Modeling of Diffraction Patterns Based on Microstructural Properties*, Eötvös University Budapest, 2008.
- [69] A. Heczeli, M. Kawasaki, J.L. Lábár, J. il Jang, T.G. Langdon, J. Gubicza, Defect structure and hardness in nanocrystalline CoCrFeMnNi High-Entropy Alloy processed by High-Pressure Torsion, *J. Alloys Compd.* 711 (2017) 143–154, <https://doi.org/10.1016/j.jallcom.2017.03.352>.
- [70] A.D. Rollett, G.S. Rohrer, F.J. Humphreys, *Recrystallization and Related Annealing Phenomena*, 3rd Editio, Elsevier, 2017.
- [71] H.J. Leamy, H. Warlimont, The elastic behaviour of Ni-Co alloys, *Phys. Status Solidi.* 37 (1970) 523–534, <https://doi.org/10.1002/psb.19700370203>.
- [72] D.J.H. Cockayne, A theoretical analysis of the weak-beam method of electron microscopy, *Zeitschrift Fur Naturforsch. - Sect. A J. Phys. Sci.* 27 (1972) 452–460, <https://doi.org/10.1515/zna-1972-0313>.
- [73] X. Sun, S. Lu, R. Xie, X. An, W. Li, T. Zhang, C. Liang, X. Ding, Y. Wang, H. Zhang, L. Vitos, Can experiment determine the stacking fault energy of metastable alloys? *Mater. Des.* 199 (2021) 109396 <https://doi.org/10.1016/J.MATDES.2020.109396>.
- [74] S. Wei, C.C. Tasan, Deformation faulting in a metastable CoCrNiW complex concentrated alloy: a case of negative intrinsic stacking fault energy? *Acta Mater.* (2020) <https://doi.org/10.1016/j.actamat.2020.09.056>.
- [75] M. Shih, J. Miao, M. Mills, M. Ghazisaeidi, Stacking fault energy in concentrated alloys, *Nat. Commun.* 12 (2021) 3590, <https://doi.org/10.1038/s41467-021-23860-z>.
- [76] E.B. Tadmor, N. Bernstein, A first-principles measure for the twinnability of FCC metals, *J. Mech. Phys. Solids.* 52 (2004) 2507–2519, <https://doi.org/10.1016/j.jmps.2004.05.002>.
- [77] L.Y. Tian, R. Lizárraga, H. Larsson, E. Holmström, L. Vitos, A first principles study of the stacking fault energies for fcc Co-based binary alloys, *Acta Mater.* 136 (2017) 215–223, <https://doi.org/10.1016/j.actamat.2017.07.010>.
- [78] S. Zhao, G.M. Stocks, Y. Zhang, Stacking fault energies of face-centered cubic concentrated solid solution alloys, *Acta Mater.* 134 (2017) 334–345, <https://doi.org/10.1016/j.actamat.2017.05.001>.
- [79] C. Niu, C.R. LaRosa, J. Miao, M.J. Mills, M. Ghazisaeidi, Magnetically-driven phase transformation strengthening in high entropy alloys, *Nat. Commun.* 9 (2018) 1–9, <https://doi.org/10.1038/s41467-018-03846-0>.
- [80] S. Huang, H. Huang, W. Li, D. Kim, S. Lu, X. Li, E. Holmström, S.K. Kwon, L. Vitos, Twinning in metastable high-entropy alloys, *Nat. Commun.* 9 (2018) 2381, <https://doi.org/10.1038/s41467-018-04780-x>.
- [81] D.B. Williams, C.B. Carter, *Transmission Electron Microscopy: A Textbook for Materials Science*, Springer US, 2009, <https://doi.org/10.1007/978-0-387-76501-3>.
- [82] P.M. Anderson, J.P. Hirth, J. Lothe, *Theory of Dislocations*, 3rd ed., Cambridge University Press, 2017. <https://www.cambridge.org/jp/academic/subjects/engineering/materials-science/theory-dislocations-3rd-edition?format=HB&isbn=9780521864367>.
- [83] M. Ojima, Y. Adachi, Y. Tomota, K. Ikeda, T. Kamiyama, Y. Katada, Work hardening mechanism in high nitrogen austenitic steel studied by in situ neutron diffraction and in situ electron backscattering diffraction, *Mater. Sci. Eng. A*. 527 (2009) 16–24, <https://doi.org/10.1016/j.msea.2009.07.066>.
- [84] Y. Wang, B. Liu, K. Yan, M. Wang, S. Kabra, Y.L. Chiu, D. Dye, P.D. Lee, Y. Liu, B. Cai, Probing deformation mechanisms of a FeCoCrNi high-entropy alloy at 293 and 77 K using in situ neutron diffraction, *Acta Mater.* 154 (2018) 79–89, <https://doi.org/10.1016/j.actamat.2018.05.013>.
- [85] A.A. Saleh, E.V. Pereloma, B. Clausen, D.W. Brown, C.N. Tomé, A.A. Gazder, Self-consistent modelling of lattice strains during the in-situ tensile loading of twinning induced plasticity steel, *Mater. Sci. Eng. A*. 589 (2014) 66–75, <https://doi.org/10.1016/j.msea.2013.09.073>.
- [86] B. Cai, B. Liu, S. Kabra, Y. Wang, K. Yan, P.D. Lee, Y. Liu, Deformation mechanisms of Mo alloyed FeCoCrNi high entropy alloy: in situ neutron diffraction, *Acta Mater.* 127 (2017) 471–480, <https://doi.org/10.1016/j.actamat.2017.01.034>.
- [87] J.S. Jeong, W. Woo, K.H. Oh, S.K. Kwon, Y.M. Koo, In situ neutron diffraction study of the microstructure and tensile deformation behavior in Al-added high manganese austenitic steels, *Acta Mater.* 60 (2012) 2290–2299, <https://doi.org/10.1016/j.actamat.2011.12.043>.
- [88] S.M. Copley, B.H. Kear, The dependence of the width of a dissociated dislocation on dislocation velocity, *Acta Metall.* 16 (1968) 227–231, [https://doi.org/10.1016/0001-6160\(68\)90118-1](https://doi.org/10.1016/0001-6160(68)90118-1).
- [89] H.J. Kestenbach, The effect of applied stress on partial dislocation separation and dislocation substructure in austenitic stainless steel, *Philos. Mag.* 36 (1977) 1509–1515, <https://doi.org/10.1080/14786437708238531>.

- [90] B.S. Lee, Y. Koizumi, H. Matsumoto, A. Chiba, Collective behavior of strain-induced martensitic transformation (SIMT) in biomedical Co-Cr-Mo-N alloy polycrystal: an ex-situ electron backscattering diffraction study, *Mater. Sci. Eng. A*. 611 (2014) 263–273, <https://doi.org/10.1016/j.msea.2014.05.071>.
- [91] S. Picak, P. Singh, D. Salas, M.A. Tunes, X. Fang, L. Zhou, M.J. Kramer, Y. I. Chumlyakov, D.D. Johnson, R. Arroyave, Y. Ren, I. Karaman, Orientation dependence of the effect of short-range ordering on the plastic deformation of a medium entropy alloy, *Mater. Sci. Eng. A*. (2023) 145309, <https://doi.org/10.1016/J.MSEA.2023.145309>.
- [92] T.M. Smith, M.S. Hooshmand, B.D. Esser, F. Otto, D.W. McComb, E.P. George, M. Ghazisaeidi, M.J. Mills, Atomic-scale characterization and modeling of 60° dislocations in a high entropy alloy, *Acta Mater.* 110 (2016) 352–363, <https://doi.org/10.1016/j.actamat.2016.03.045>.
- [93] S.I. Rao, C. Woodward, T.A. Parthasarathy, O. Senkov, Atomistic simulations of dislocation behavior in a model FCC multicomponent concentrated solid solution alloy, *Acta Mater.* 134 (2017) 188–194, <https://doi.org/10.1016/j.actamat.2017.05.071>.
- [94] S. Nag, W.A. Curtin, Effect of solute-solute interactions on strengthening of random alloys from dilute to high entropy alloys, *Acta Mater.* 200 (2020) 659–673, <https://doi.org/10.1016/j.actamat.2020.08.011>.
- [95] W.G. Nöhring, W.A. Curtin, Dislocation cross-slip in fcc solid solution alloys, *Acta Mater.* 128 (2017) 135–148, <https://doi.org/10.1016/j.actamat.2017.02.027>.
- [96] W.G. Nöhring, W.A. Curtin, Cross-slip of long dislocations in FCC solid solutions, *Acta Mater.* 158 (2018) 95–117, <https://doi.org/10.1016/j.actamat.2018.05.027>.
- [97] S.I. Hong, C. Laird, Mechanisms of slip mode modification in F.C.C. solid solutions, *Acta Metall. Mater.* 38 (1990) 1581–1594, [https://doi.org/10.1016/0956-7151\(90\)90126-2](https://doi.org/10.1016/0956-7151(90)90126-2).
- [98] S.I. Hong, Criteria for predicting twin-induced plasticity in solid solution copper alloys, *Mater. Sci. Eng. A*. 711 (2018) 492–497, <https://doi.org/10.1016/j.msea.2017.11.076>.
- [99] J.W. Christian, S. Mahajan, Deformation twinning, *Prog. Mater. Sci.* 39 (1995) 1–157, [https://doi.org/10.1016/0079-6425\(94\)00007-7](https://doi.org/10.1016/0079-6425(94)00007-7).
- [100] J.-S. Hong, S. Kang, J.-G. Jung, Y.-K. Lee, The mechanism of mechanical twinning near grain boundaries in twinning-induced plasticity steel, *Scr. Mater.* 174 (2020) 62–67, <https://doi.org/10.1016/j.scriptamat.2019.08.025>.
- [101] S. Miura, J. Takamura, N. Narita, Orientation dependence of the flow stress for twinning in silver crystals, *Trans. JIM.* 9 (1968) 555.
- [102] N. Narita, J. Takamura, Deformation twinning in F.C.C. and B.C.C. metals, in: F.R. N. Nabarro (Ed.), *Dislocations Solids*, 1992, pp. 135–189. Vol. 9.
- [103] N. Narita, J. Takamura, Deformation twinning in silver- and copper-alloy crystals, *Philos. Mag.* 29 (1974) 1001–1028, <https://doi.org/10.1080/14786437408226586>.
- [104] M. Schneider, E.P. George, T.J. Manescau, T. Zálezák, J. Hunfeld, A. Dlouhý, G. Eggeler, G. Laplanche, Analysis of strengthening due to grain boundaries and annealing twin boundaries in the CrCoNi medium-entropy alloy, *Int. J. Plast.* 124 (2020) 155–169, <https://doi.org/10.1016/j.ijplas.2019.08.009>.